



Seismic performance of Fe-SMA prestressed segmental bridge columns with 3D printed permanent concrete formwork

Saim Raza^a, Zafiris Triantafyllidis^a, Ana Anton^b, Benjamin Dillenburger^b,
Moslem Shahverdi^{a,c,*}

^a Empa, Swiss Federal Laboratories for Materials Science and Technology, Dübendorf 8600, Switzerland

^b Institute of Technology in Architecture, D-ARCH, ETH Zurich, Stefano-Franscini-Platz 1, Zürich 8093, Switzerland

^c School of Civil Engineering, University of Tehran, Tehran 4563-11155, Iran

ARTICLE INFO

Keywords:

Accelerated bridge construction
Prefabricated segmental columns
Self-centering seismic behavior
3D printed concrete formwork
Shape memory alloy prestressing

ABSTRACT

The integration of digital fabrication technology with prestressed segmental column construction offers significant potential for accelerated bridge construction with material-efficient design. This study aims to explore this potential by developing a novel prestressed segmental column system that utilizes permanent 3D printed concrete (3DPC) formwork for column segment fabrication. Prestressing is achieved in the proposed system by using partially bonded iron-based shape memory alloy (Fe-SMA) reinforcement. Large-scale experiments were conducted on two columns under combined gravity and lateral loading to evaluate the seismic performance and feasibility of the proposed system. The ratio of steel to Fe-SMA reinforcement in the column design was the variable considered in this study. The experimental results showed that the columns could withstand lateral drifts of up to 5% without collapse and the permanent 3DPC formwork showed no premature failure or delamination. Furthermore, the columns exhibited self-centering characteristics, maintaining a residual drift of 1% up to a target drift of 4% when the reinforcement ratio of steel to Fe-SMA rebars was 0.3. The results highlight the potential of the proposed prefabrication concept in designing material-efficient and seismically resilient bridge columns with low damage characteristics.

1. Introduction

The use of precast concrete in bridge construction has witnessed a significant increase in recent years due to its numerous advantages, including accelerated construction, better quality control, reduced labor requirements, and minimal traffic disruption. The emergence of digital fabrication technology has further opened up possibilities to accelerate the prefabrication process by using formwork fabricated with 3D printed concrete (3DPC) [1,2]. 3DPC enables the fabrication of complex geometries in less time and eliminates the need for temporary formwork, which can account for up to 35–60% of the total construction cost [3]. Additionally, 3DPC formwork can significantly reduce construction waste compared to conventional timber formwork, which accounts for up to 30% of the total construction waste generated [4]. Recent research studies and field practice have demonstrated the successful use of stay-in-place 3DPC formwork in reinforced concrete (RC) columns [5–9], walls [10] and ultra high performance concrete (UHPC) formwork for beams [11], whereas there have been recent proposals for using

3DPC to enable sustainable, structurally efficient (and otherwise complex to manufacture) beams, ribbed concrete slabs and floor systems [12–14]. The use of permanent 3DPC formwork offers immense potential for designing material-efficient structures and further accelerating bridge construction, particularly in the context of large-scale infrastructure projects where concrete cannot be replaced by other materials [15].

Segmental construction with precast units is not a new concept in bridge engineering, as it was first introduced in the mid-1940 s by Eugène Freyssinet, and it became one of the standard construction methods globally after 1960 s with the introduction of match-cast segment joints [16]. However, the application of this method has been limited for many decades only to bridge superstructures. Some of the first applications of prefabricated segmental bridge piers and column systems were realized in the mid-1990 s in the United States [17,18] and rapidly gained attention as an effective method towards modular and accelerated bridge construction. Due to prefabrication and rapid assembly on site, construction time can be reduced to approximately 50%

* Corresponding author at: Empa, Swiss Federal Laboratories for Materials Science and Technology, Dübendorf 8600, Switzerland.

E-mail addresses: moslem.shahverdi@ut.ac.ir, moslem.shahverdi@empa.ch (M. Shahverdi).

<https://doi.org/10.1016/j.engstruct.2023.117423>

Received 28 June 2023; Received in revised form 24 November 2023; Accepted 21 December 2023

Available online 2 January 2024

0141-0296/© 2023 The Author(s). Published by Elsevier Ltd. This is an open access article under the CC BY license (<http://creativecommons.org/licenses/by/4.0/>).

of that in cast-in-place bridge pier construction [19], with clear benefits with regards to reducing construction costs, disruption time and environmental footprint. Noteworthy applications of precast segmental bridge columns include the Louetta Road Overpass in Houston and the Victoria Bridge in New Jersey, USA; further examples and an overview of precast bridge column design solutions can be found in [20]. These columns typically consist of prefabricated segments manufactured off-site and assembled on-site along with the footing and cap beam. Prestressing is provided by unbonded tendons to ensure the integrity of all column components.

A distinctive characteristic of the prestressed segmental columns is that the interface between the segments acts as a pre-crack under lateral loading, resulting in an opening under tensile stresses. This behavior, which typically occurs at the interface between the footing and bottom column segment, allows the columns to exhibit controlled rocking under lateral loading, enabling the columns to return to their original position under the action of the restoring force provided by the prestressed tendons, thereby enabling self-centering characteristics. However, these columns exhibit limited hysteretic energy dissipation [21,22]. To overcome this limitation, various systems have been proposed. Some studies have explored the use of mild steel rebars, known as energy-dissipating (ED) rebars, which extend continuously through the footing and column segments to enhance energy dissipation [23–27]. More recently, an innovative system consisting of a traditional inner column inside a precast column has been proposed to increase energy dissipation [28]. Other studies have used external steel plates for increasing energy dissipation [29,30]. Additionally, the performance of bonded and unbonded prestressing tendons has been compared, with findings suggesting that bonded tendons result in higher residual drifts due to prestressing losses caused by significant strains in the bonded tendons [31]. However, it is important to note that the use of fully unbonded tendons may increase the corrosion potential.

The conventional prestressing procedure for segmental columns, involving the use of post-tensioned wire tendons, is a complex process, requiring the operation of heavy mechanical equipment onsite (and typically at height), such as hydraulic jacks, anchor heads, etc. An attractive alternative to simplify this process is the utilization of iron-based shape memory alloy (Fe-SMA) rebars for prestressing. Fe-SMA belongs to a class of smart materials with the unique ability to recover inelastic deformations upon heating. This ability, which is known as the shape memory effect and is due to microstructural phase transformations of the alloy upon thermomechanical stimulus, can be used to generate prestress in Fe-SMA reinforcement by preventing strain recovery through end anchorage [32]. Electric resistive heating or gas flame activation can be used to heat the Fe-SMA reinforcement within RC structures. Fe-SMA reinforcement has been successfully utilized in various structural applications [33], including flexural strengthening of RC beams and slabs [34–39] and shear strengthening of RC beams [40–42]. Experimental investigations have also explored the bond behavior of embedded [43], near-surface-mounted [44–46], and post-installed [47] Fe-SMA rebars. The characterization of the recovery stress behavior of Fe-SMA under cyclic load reversals has been carried out by [48]. Some recent studies have also focused on increasing the recovery stress and yield stress of Fe-SMA [49–51], which are in the range of 300 MPa and 400 MPa, respectively for the existing alloy [33]. More recently, nonlinear finite element modelling has been used to investigate the behavior of Fe-SMA-reinforced concrete structures [52–54]. The application of Fe-SMA to new bridge piers has not yet been realized; however, Ni-Ti based SMA rebars have been used in the past to improve the self-centering properties of RC bridge piers [55,56]. The seismic performance of segmental columns using superelastic SMA bolts and steel angles has been investigated, where SMA and steel contribute to self-centering and energy dissipation, respectively [57]. More recently, innovative concepts for bridge piers have been proposed for damage control and self-centering behaviour using superelastic Ni-Ti-based SMA washers as kernel elements for rocking bridge piers

[58,59]. Fang [60] has provided a comprehensive review of the applications of SMAs for buildings as well as bridge structures in seismic zones.

This study aims to integrate digital fabrication technology [61,62] with segmental construction methods and a simplified prestressing technique using Fe-SMA reinforcement to fabricate prestressed segmental columns for accelerated bridge construction. The use of permanent 3DPC formwork provides the design freedom to manufacture material-efficient geometries for segmental columns, which can otherwise be challenging and labor intensive to manufacture using conventional methods. In addition, the 3DPC formwork serves as a permanent part of the structure and it can contribute to the protective cover layer of the reinforcement, unlike conventional timber formwork, which is temporary and often discarded after a few times usage, resulting in significant construction waste. To this end, this study used permanent 3DPC formwork to fabricate modular column segments, which were then assembled together and prestressed through electric resistive heating of Fe-SMA. The feasibility of the proposed system was investigated through large-scale experiments on two columns subjected to combined gravity and lateral loading. The next section provides a detailed description of the experimental programme, followed by a comprehensive analysis and discussion of the experimental results.

2. Experimental programme

2.1. Specimen design

The column specimens consisted of 4 cylindrical segments, each 380 mm in diameter and 350 mm in height. The total column height was 1400 mm and represented a 1:4 scale model of a typical bridge pier. The primary design criteria for the columns were to ensure low damage and self-centering characteristics, together with some energy dissipation. Specimen S1 was reinforced with 2 ϕ 14 continuous steel rebars and 6 ϕ 14 discontinuous steel rebars in each segment, as shown in Fig. 1(a) and (c). In contrast, specimen S2 was reinforced with 4 ϕ 14 continuous steel rebars and 4 ϕ 14 discontinuous steel rebars, as shown in Fig. 1(b) and (c). Note that continuous steel rebars extend continuously from the footing to the column head, whereas discontinuous steel rebars are installed in individual segments. From here onwards, the continuous steel rebars will be referred to as ED steel rebars for simplicity. 4 ϕ 18 Fe-SMA rebars were used for prestressing in both columns. It is typically recommended that for self-centering, the contribution of post-tensioned reinforcement to the total bending moment resistance should be higher than that of the ED rebars [63]. Considering this, the study used two ED steel to Fe-SMA reinforcement ratios ($\frac{P_{ED}}{P_{SMA}}$) i.e. 0.3 (for specimen S1) and 0.6 (for specimen S2) to study the self-centering and energy dissipation characteristics of the proposed column system.

In both columns, the cylindrical 3DPC formwork in each segment consisted of a single filament that had a thickness of 20 mm and a layer height of 10 mm. These dimensions were selected such that the filament stability and geometry control is ensured during printing for the particular printer setup and material. Furthermore, the thickness was kept as low as practically possible, in order to minimize the ratio of 3DPC to cast-in-place concrete area for the given column cross-section. This was to ensure that the sustainability of the columns is not adversely affected by the use of 3DPC, since current 3DPC materials contain relatively high cement dosages (and associated CO₂ emissions) compared to conventional large-aggregate concrete mixes [64].

Corrugated ducts of ϕ 30 were provided in the column segments to allow the post-installation and grouting of ED steel and Fe-SMA rebars as shown in Fig. 1(c). A shrinkage-compensated high-strength mortar of type SikagROUT 311 [65], with a maximum aggregate size of 1 mm, was used for grouting ED steel and Fe-SMA rebars into the corrugated ducts. The Fe-SMA rebars had a plain (smooth) middle region to allow partial bonding with the grout to delay yielding and loss of prestress and

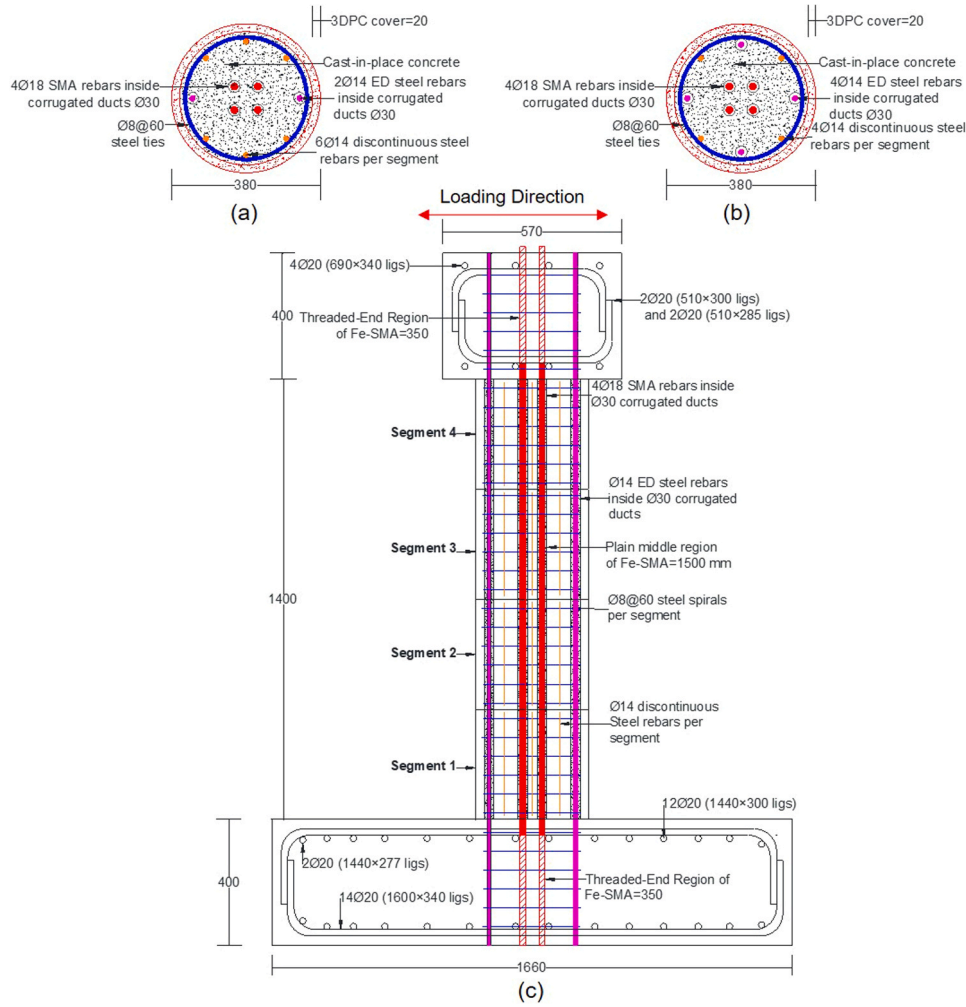


Fig. 1. Design details of columns (all dimensions in mm): a) S1 cross-section; b) S2 cross-section; c) front elevation.

threaded end regions for anchorage into the cast-in-place footing and top loading block. The length of the threaded end anchorage region was selected as 20 times the rebar diameter, d_b based on the findings of [47]. Note that the plain portion of Fe-SMA rebars extended 50 mm below the footing-column interface to enable a controlled rocking mechanism. The column ties consisted of $\phi 8 @ 60$ mm steel, corresponding to limited ductile confinement for concrete bridges according to EN 1998-2 [66]. The dimensions of the footing and top loading block were $1660 \times 1500 \times 400$ mm and $570 \times 750 \times 400$ mm, respectively.

The design details of the columns are summarized in Table 1. The mean compressive cube strength of 3DPC mortar, cast concrete and Sikagrout was determined on the day of large-scale experiments on columns. A high-strength concrete class was specified for the proposed column system for two reasons: (i) to be compatible with the typical high strength of two-component (2K) 3DPC mortars, and (ii) to allow reductions in column size to save material, resulting in lightweight columns with relatively high load capacity. The modulus of elasticity and flexural strength of 3DPC mortar and Sikagrout were determined using

Table 1
Test matrix.

No.	Compressive Strength (f_{cu}) MPa			Longitudinal Reinforcement (ρ_l , %)		Steel Spirals (mm) (ρ_s , %)	Axial Load Ratio ($P_{P,G}/A_g f_c$)	
	3DPC Formwork	Cast Concrete	Grout	ED Steel	Fe-SMA		Prestress P_P (kN)	Gravity Load P_G (kN)
S1	84	87	89	2Ø14 (0.27%)	4Ø18 (0.9%)	Ø8 @60 (1.05)	282 (0.036)	468 (0.057)
S2	84	87	89	4Ø14 (0.54%)	4Ø18 (0.9%)	Ø8 @60 (1.05)	294 (0.037)	468 (0.057)

where, f_{cu} = mean compressive cube strength; f_c = mean compressive cylindrical strength; ρ_l = longitudinal reinforcement ratio; ρ_s = volumetric ratio of transverse reinforcement relative to the concrete core; P_P = prestressing load; P_G = gravity load

40 × 40 × 160 mm prisms. The moduli of elasticity of the 3DPC mortar and Sikagrout were 28 GPa and 31 GPa, respectively, and the flexural strengths were 8 MPa and 11 MPa, respectively. In relation to the interaction between printed and cast concrete, previous studies have reported that the mechanical interlock between printed and cast concrete due to the ribbed topology of 3DPC results in a good bond and prevents premature separation [5]. Thus, in addition to adhesion, the bond between 3DPC and cast concrete in the current study was due to the interlocking of the cast concrete between successive layers of printed concrete, which have an undulating surface finish due to the free flow filament deposition off the printer nozzle.

Grade B500B steel reinforcement with a specified yield strength of $f_y = 500$ MPa and an ultimate strain at failure (ϵ_u) of 5% was used as longitudinal and transverse reinforcement. The elastic modulus, yield strength, ultimate strength, and failure strain of the prestressed Fe-SMA rebars used in this study were 75–100 GPa, 400 MPa, 800 MPa, and 40%, respectively. The Fe-SMA rebars had an initial prestrain of 4%.

2.2. Construction and assembling procedure

Fig. 2 illustrates the various steps involved in the construction and assembly of the columns. 3D-printed cylindrical shells were fabricated using an extrusion-based robotic concrete printer, as shown in Fig. 2(a), and were used as the stay-in-place formwork for the prefabricated column segments. The reinforcement cage, consisting of discontinuous steel rebars, ties, and corrugated steel ducts, was then installed in the hollow 3DPC formwork, as shown in Fig. 2(b). The ducts were provided to allow for the connection between the footing and precast column segments via ED steel and Fe-SMA rebars. Cast concrete was then poured into the segments, as shown in Fig. 2(c). The segments were then stacked over the precast footing shown in Fig. 2(d). Some cement paste was used

at segment interfaces to allow bonding between the segments, as shown in Fig. 2(e). The ED steel and Fe-SMA rebars were then grouted, as shown in Fig. 2(f). The assembled column segments are shown in Fig. 2(g). Finally, the top loading block was cast as shown in Fig. 2(h).

2.3. Activation of Fe-SMA rebars and column prestressing

Electric resistance heating was used to activate the embedded Fe-SMA rebars to generate recovery stress and prestress the column. The purpose of the prestressing was two-fold — to hold the segments together and to add self-centering characteristics to the column. To enable easy access for connecting the power supply for heating, each pair of Fe-SMA rebars was connected into a single continuous conductor before concrete casting. This was achieved by welding a short horizontal piece of the same type of rebar halfway through their embedded length in the footing, as shown in Fig. 3(a) so that each pair of rebars can be activated simultaneously by having connection points only from above. At the top of the column, Fe-SMA rebars protruded by a length of 100 mm for clamping the power supply connectors, as shown in Fig. 3(b). After activation and prior to structural testing, these rebars were cut flush with the concrete surface to allow attachment of the vertical load actuator.

A bespoke electric power supply was used to pass a direct current of 535 A at 12.2 V from each connected pair of rebars. The duration of resistive heating was controlled by the maximum temperature reached at the rebar surface. After that, the power was switched off and the rebars cooled down by dissipating heat to the surrounding concrete. Three thermocouples of type K were attached at three different locations throughout the length of each rebar for regular temperature control. The thermocouples were attached to the rebars before the segments were assembled and grouted.

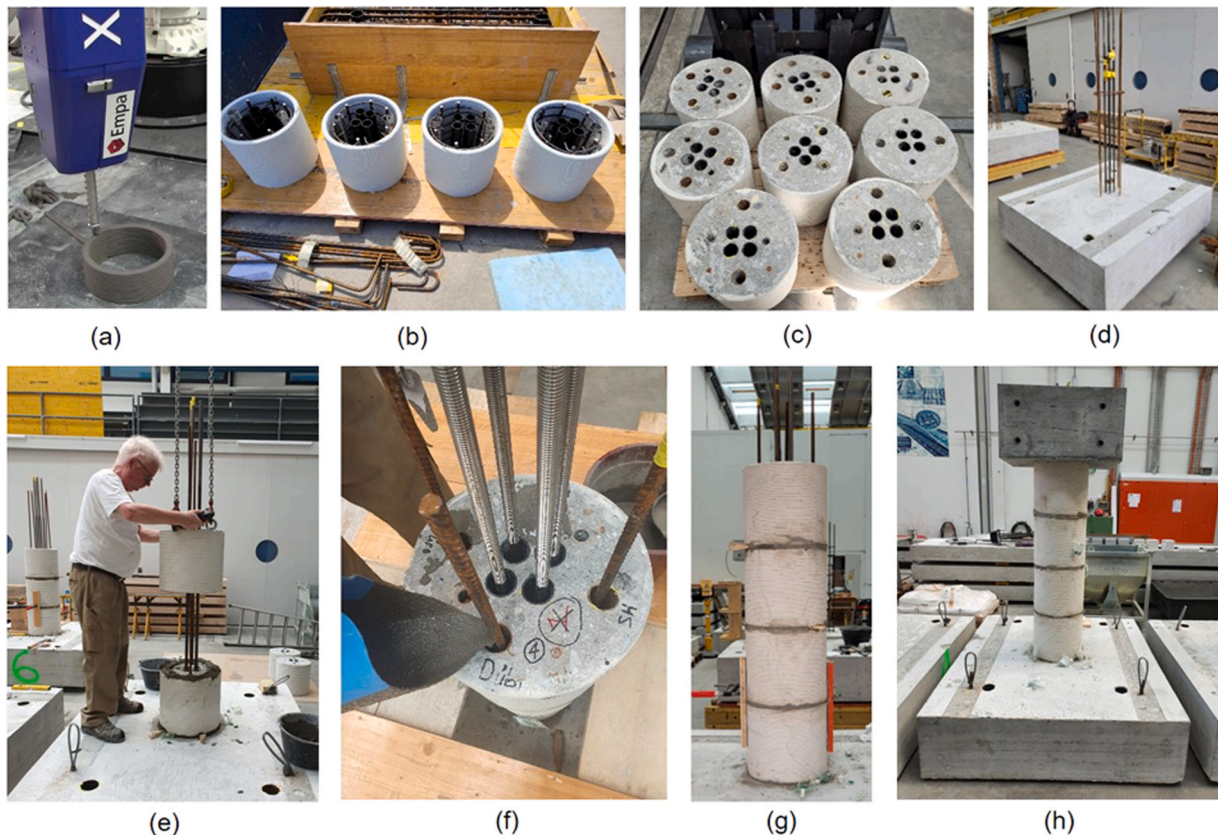


Fig. 2. Construction and assembly procedure: a) fabrication of hollow 3DPC formwork shells; b) installation of reinforcement cage and ducts in segments; c) segments filled with cast concrete; d) cast footing with continuous ED steel and Fe-SMA rebars; e) stacking of segments over footing; f) grouting of ED steel and Fe-SMA rebars; g) assembled column segments; h) completed column assembly with top loading block.

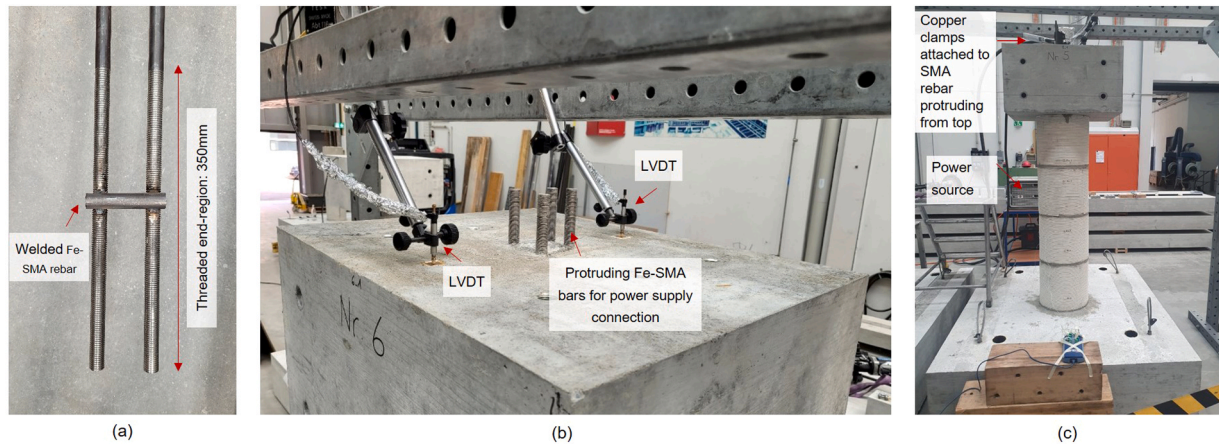


Fig. 3. Setup for Fe-SMA activation by electrical resistance heating: (a) rebar pair joint within column footing for electrical continuity; (b) protruding Fe-SMA rebars acting as electrical connection points and axial displacement measurement instrumentation; (c) overall activation setup.

Axial displacements during prestress development from Fe-SMA rebar activation were monitored with two linear variable displacement transducers (LVDTs) with a stroke of 5 mm, which were attached to the column head and mounted on a rigid steel frame that was constructed around the columns, as shown in Fig. 3(b) & (c). The axial displacements of the column were measured for 20 h after activation.

2.4. Loading setup and instrumentation

The experimental setup used for column testing under combined axial compression and quasi-static lateral loading is shown in Fig. 4. The experimental setup comprised a steel reaction frame and two hydraulic actuators. The gravity load was applied to the column by a Hydrel 2MN actuator, while the lateral load was induced using a Schenck 630 kN actuator with a stroke capacity of ± 200 mm. The vertical actuator was connected to the steel reaction frame and top loading block of the column using a pin connection to allow for free rotation of the vertical actuator under the column's lateral displacement. This arrangement resulted in the tilting of the vertical actuator at large lateral displacements, thereby inducing an additional horizontal load component to the column. This additional horizontal load was added to the obtained lateral load-displacement hysteresis during the post-processing of results. A pin connection was used to connect the horizontal actuator to

the column loading block. The other end of the horizontal actuator was bolted to the rigid steel reaction frame. A digital 2-channel control system (Walter+Bai PCS 8000), was used for controlling the hydraulic actuators. The column footing was fixed to the laboratory's strong floor using four M60 bolts, each prestressed to 1MN.

Fig. 4(b) shows the schematics of the instrumentation used during the experiments. The instrumentation comprised 13 displacement transducers consisting of LVDTs, string potentiometers (SPOTs), and a laser transducer. The lateral displacement at the column tip was controlled using a laser-based transducer. Additionally, lateral displacement at the horizontal actuator location was measured using a SPOT for comparison with the actuator stroke measurement. The average axial displacement of the column centerline was determined from the measurements of four SPOTs attached to the corners of the top loading block. The joint opening between the Footing and Segment 1 and between Segment 1 and Segment 2 was measured with LVDTs mounted at the respective locations on the push and pull loading faces of the column (Fig. 4b). The potential slip and rocking of the column footing were also monitored using LVDTs. In addition to the physical instrumentation, Digital Image Correlation (DIC) (VIC-3D system, Correlated Solutions) was used to monitor the damage progression in the lower 500 mm of the column, as shown in Fig. 4(b).

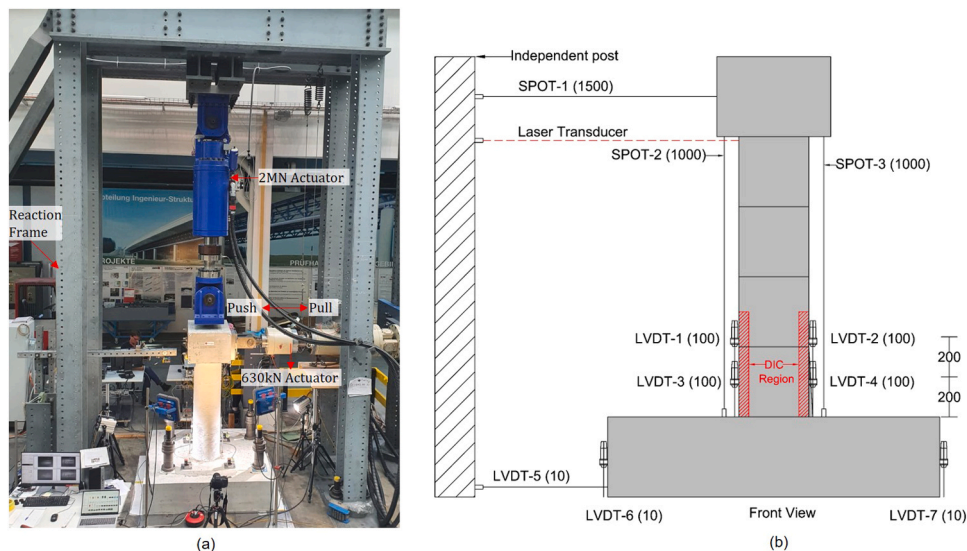


Fig. 4. a) Loading setup; b) instrumentation (measurement ranges in mm).

2.5. Loading protocol

The experiments were conducted under constant axial load and incrementally increasing quasi-static lateral displacements. The constant axial load represented the dead load on the bridge pier from the superstructure. The lateral loading protocol represented the displacements imposed at the tip of bridge columns as a result of ground motion excitations. The axial load was applied at the beginning and maintained constant throughout the experiment. The specimens were subjected to a constant axial load ratio of 0.057. The lateral loading was displacement-controlled and consisted of drift increments of $\pm 0.2\%$, $\pm 0.4\%$, $\pm 0.6\%$, $\pm 1\%$, $\pm 2\%$, $\pm 3\%$, $\pm 4\%$, $\pm 5\%$, as shown in Fig. 5, applied at a rate of 10 mm/min. The amplitude of the displacement excursions was selected to develop an understanding of the full range elastic and inelastic behavior of the proposed column system under seismic actions. The smaller displacement excursions $\leq \pm 1\%$ were intended to provide an understanding of the elastic response and yielding behavior of the column, whereas the displacement excursions $\geq \pm 1\%$ were intended to elucidate the peak and post-peak behavior of the proposed column system. Each loading cycle was repeated twice to capture the strength and stiffness degradation of the specimens. The experiment was stopped at 5% drift due to the limitations of the loading setup.

3. Results and discussion

3.1. Estimation of prestress generated from Fe-SMA activation

The initial prestress generated in the column was estimated using the measured axial deformations resulting from the activation. Fig. 6(a) and (b) show the temperature evolution of the Fe-SMA rebar during activation and the resulting deformations, for columns S1 and S2, respectively. As mentioned previously, the four Fe-SMA rebars in each column were electrically connected in pairs and the prestress activation consisted of two resistive heating rounds. With the applied current density, the first rebar pair of each column reached the target temperature of 180°C within approximately 10–11 min, when the power supply was switched off and the rebars started to cool down slowly by conducting heat to the surrounding grout and concrete (this is indicated also by the mild temperature increase in the second rebar pair, during the cooling phase of pair 1 upon switching off the power supply). Current injection in the second rebar pair of Specimen S1 initiated 10 min after the power supply was stopped at the first rebar pair, which by that time had cooled

down to approximately 75°C . The duration to reach the target rebar temperature of 180°C in the second rebar pair of each column and stop the power supply was 8–9 min. A similar procedure was repeated for specimen S2. It is worth noting here that the overall activation procedure for both columns (i.e. all four heating rounds) lasted one hour, with an additional time of 5 min before and 5 min after the heating process for setting up/removing cable leads and connectors. The total energy consumed for both specimens was 4.15 KWh. This highlights the benefits of this prestressing technique including ease and speed of application.

The target activation temperature was chosen as 180°C , so that a sufficiently high recovery stress is generated in the Fe-SMA rebar without causing damage to the surrounding concrete. Although no additional thermocouples were used to measure the concrete temperature in the vicinity of the rebars (to avoid the clutter of sensor cables during the fabrication and assembly of segments), a 2D transient heat transfer analysis was performed in Abaqus FEA to examine the effects of heat dissipation in concrete. The thermal analysis assumed that the total cross-section comprised of conventional concrete (i.e. potential differences in the thermal properties of grout and 3DPC were assumed negligible, due to the unavailability of relevant data), whereas the effects of ED steel rebars and corrugated steel ducts were also neglected. The analysis considered the temperature-dependent thermal properties for normal weight concrete and the convective and radiative heat transfer coefficients provided in Eurocode [67,68]. The predicted temperature fields indicated that for the applied rebar heating amplitude the temperature increase in the cast-in-place concrete was minor. Therefore, no mechanical degradation is practically expected in the load-bearing cast concrete infill due to temperature effects. On the other hand, higher localized peak temperatures were reached in the region of the four grouted Fe-SMA rebar ducts. Although there is a likelihood of microcracking in concrete and cementitious grouts in this region, the effects of potential microcracking in the grout due to mechanical degradation and restrained thermal expansion are insignificant, since partial bond of the plain (smooth) Fe-SMA rebars was an intentional design consideration, as described above.

The evolution of the column total axial deformations upon heating and cooling are shown in Fig. 6. The stepwise heating/activation is clearly noticeable in the measured responses, which show coincident displacement reversals at the instant of stopping and restarting the current/heat input in each rebar pair. When heating started, the columns experienced elongation initially due to pure thermal expansion of the Fe-SMA rebars up to the temperature range of $40\text{--}50^\circ\text{C}$, since activation of shape memory initiates beyond this temperature range [32]. However, the columns continued to elongate thereafter despite triggering the reversal of martensitic transformation in the alloy, but with a noticeable reduction in elongation rate. This is because phase transformation and shape recovery occurs gradually in Fe-SMA upon heating and the full recovery stress develops only after the rebar has cooled down to ambient temperature, when thermal stresses due to restrained expansion have fully recovered [32]. Nonetheless, recovery stress develops rapidly during the cooling phase; indicatively, the stress in the Fe-SMA rebar, when it cools down to 100°C , is approximately 70% of the full recovery stress value at ambient temperature [32].

Despite the immediate reversal of displacement measurements upon switching off the power supply/heat input in both rebar pairs, Fig. 6 shows that the total axial displacement of the columns remained positive (i.e. expansion) for a substantial duration (3 h) after the resistive heating of rebars stopped, whereas the columns contracted slowly, even though a significant proportion of the full prestress load was already activated. This happened owing to the combined effect of thermal expansion of concrete and Fe-SMA rebars as a result of the rise in temperature. The heat that is rapidly generated from the Joule phenomenon in the Fe-SMA flows into the surrounding grout and further into the cast-in-place concrete by conduction, as a result of the thermal gradient between the hot rebars and the cool concrete cross-section. However,

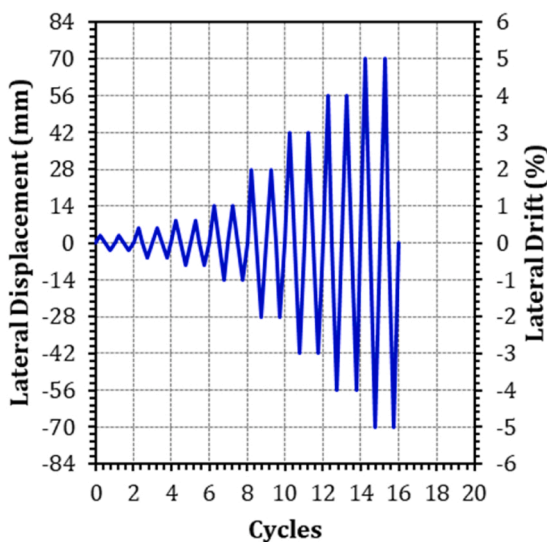


Fig. 5. Incrementally increasing displacement-controlled lateral loading protocol.

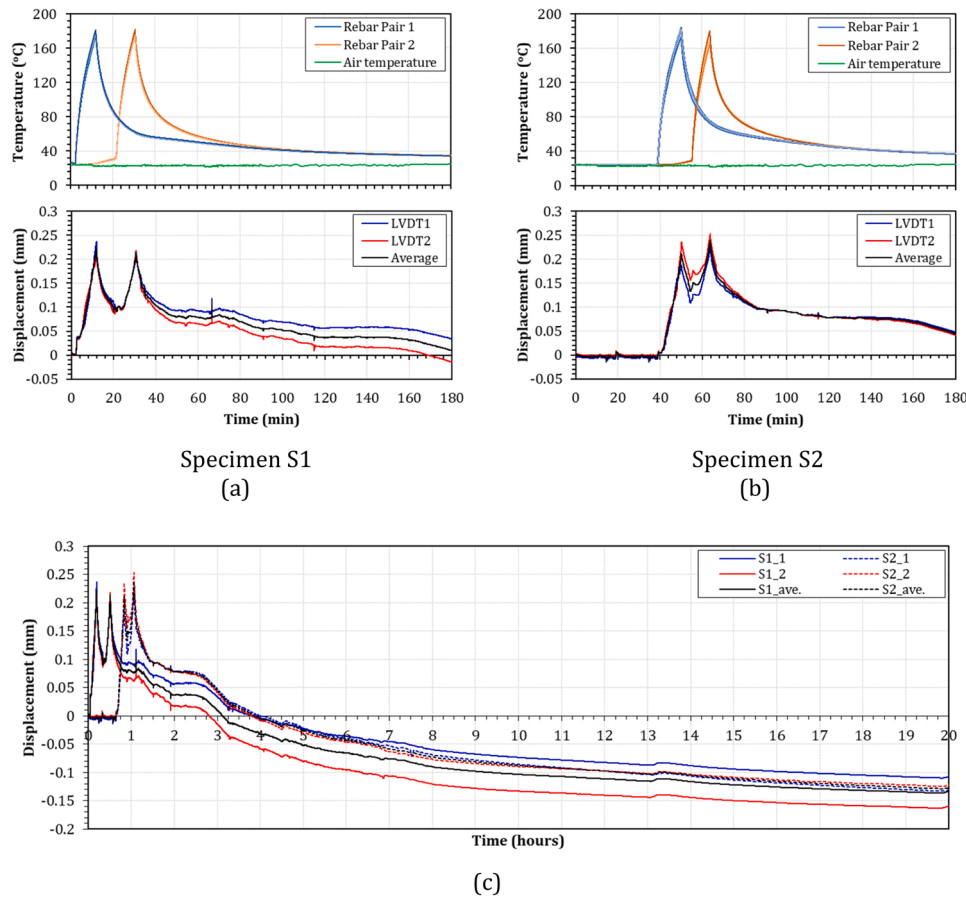


Fig. 6. Evolution of temperature and axial displacement in the first 3 h after activation for (a) S1; (b) S2; and (c) long-term axial displacements for S1 and S2 for 20 h after activation.

temperatures within concrete columns change slowly in general, because of the low thermal conductivity of concrete and the high thermal massivity of cross-sections. Furthermore, temperatures continue to rise away from the heated surface (in this case, the rebar-concrete interface) even after heat input is stopped and cooling begins, until thermal gradients cease to exist within the cross-section [69]. Hence, the total deformation measured by the LVDTs at the surface of the columns' top loading block at any instant is due to the combination of prestressing effects, creep, and the thermal expansion of concrete and Fe-SMA, until the cross-section returns to ambient temperature and thermal expansion is recovered.

Therefore, the final axial stress acting on the concrete due to prestressing was determined from the average axial strain after 20 h from activation, when the measured temperatures approached thermal equilibrium with ambient air. Axial strain at the centerline of the column was determined as the average of the two LVDT displacement measurements, over a length of 1800 mm. The effects of creep in the measured total axial displacement were included by following the provisions of EN 1992-1-1[70] for estimating the creep coefficient and resulting creep strains of concrete, based on the age of the columns (88

days) at the time of loading. The total axial deformation of the column was accordingly adjusted to determine deformation due to prestress.

Table 2 compares the estimated axial stress determined from the axial displacement with the theoretical axial stress expected to be generated in the columns, assuming a recovery stress of 300 MPa in each rebar on thermal activation at 180° C. The theoretical axial stress took into account the loss of recovery stress due to the elastic shortening of the concrete, which was estimated to be 5 MPa per rebar. The results show that the estimated axial stress in specimens S1 and S2 were similar and in good agreement with the theoretical axial stress, indicating that the prestress from Fe-SMA activation was generated in the column, as intended.

3.2. General column response and cracking patterns

The columns exhibited a controlled-rocking behavior with joint openings at the Footing-to-Segment 1 and Segments 1-to-2 interfaces, whereas no rocking or slip occurred at the interface of footing and strong floor. Horizontal flexural cracking occurred at the Footing-to-Segment 1 and Segments 1-to-2 interfaces at low drifts, leading to joint openings at

Table 2
Estimated initial prestress in columns after 20 h of activation.

No.	Total Axial Deformation (mm)	Creep Deformation (mm)	Axial Deformation due to prestressing (mm)	Estimated Axial Stress on Concrete (MPa)	Theoretical Axial Stress on Concrete* (MPa)
S1	0.133	0.02	0.113	2.45	2.5
S2	0.127	0.02	0.107	2.33	2.5

* Based on an effective recovery stress of 300 MPa at 180° C.

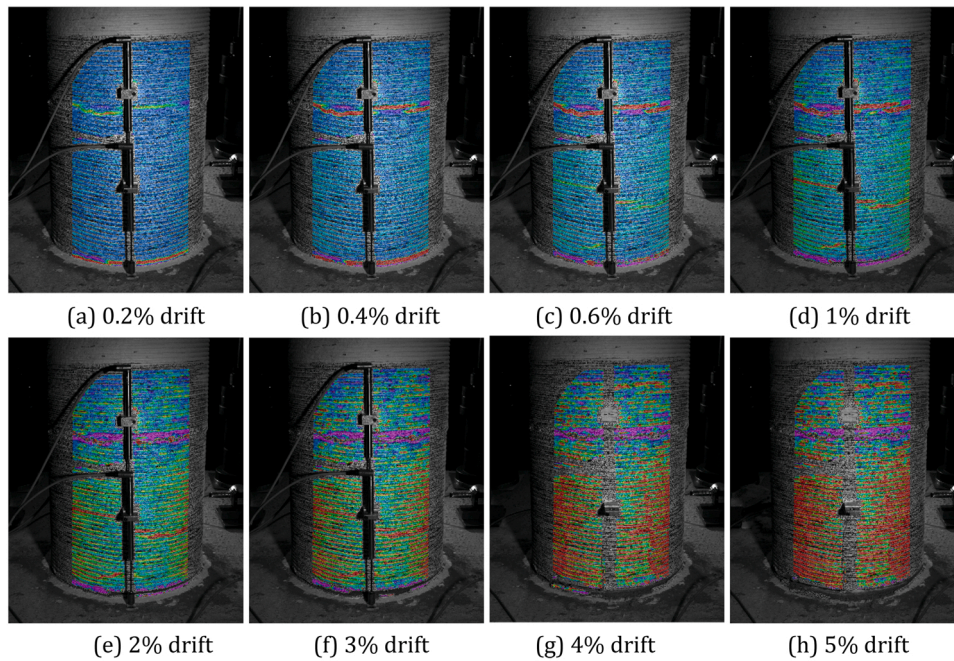


Fig. 7. Axial strain patterns in specimen S1 under tension load reversals at different drift levels on loading face in push direction.

higher drifts. Vertical splitting of the 3DPC formwork occurred at drifts $\geq 4\%$. No visible cracking was observed at the Segments 2-to-3 and Segment 3-to-4 interfaces. No buckling or fracture of the ED steel or Fe-SMA reinforcement was observed.

Fig. 7 shows the axial strain patterns during the tensile load reversals in the bottom 500 mm of the 3DPC formwork of Specimen S1 as determined by DIC measurements on the loading face in the push direction. The results show strain concentration at the Footing-to-Segment 1 and Segment 1-to-2 interfaces from the very first drift excursion of 0.2%, as shown in Fig. 7(a). The horizontal crack appeared at the Footing-to-Segment 1 interface at 0.4% drift, as shown in Fig. 7(b), and led to the base joint opening at subsequent drifts, as shown in Fig. 7(c) and (d). Fig. 7(e) to (h) show that the joint opening continued to increase in size up to 5% drift when the experiment was stopped. Horizontal cracks were generally observed only at the Footing-to-Segment 1 and Segment 1-to-2 interfaces. Although some tensile strain concentration developed at mid-height of Segment 1 at 0.6% and 1% drifts, no significant cracking was visible between the layers of the 3DPC formwork. There was also no significant opening at the Segments 1-to-2 joint, other than hairline cracks on the grouted joint.

The hoop strain patterns of specimen S1 during the compression load reversals at 3%, 4%, and 5% drifts are shown in Fig. 8. It can be observed that during the compression reversals, large hoop strains developed in Segment 1 at 3% drift, as shown in Fig. 8(a). Fig. 8(b) shows that high hoop strains due to longitudinal compression led to the vertical splitting of the 3DPC formwork at 4% drift. The splitting of the formwork occurred at the extreme fiber of the loading face of Segment 1 and increased in length at 5% drift, as shown in Fig. 8(c).

When 5% drift was reached in the pull direction in S1, part of the split 3DPC formwork in the compressed column face of Segment 1 separated, buckled outwards and fell off (Fig. 9(a), (b)).

This failure seems to have been likely instigated by crushing of the 3DPC formwork, following the crushing of the cast infill concrete and spreading of the plastic hinge zone at the bottom of Segment 1. As previously mentioned, a vertical splitting crack initiated at the base of the 3DPC formwork in Segment 1 at approximately 4% drift, due to the increasing dilation of the compressed concrete core beneath the formwork. As the column rotation increases, the plasticity zone in the cast concrete propagates (as expected) inwards and upwards, and further diagonal failure planes form in the unconfined zones of the core (i.e. outside

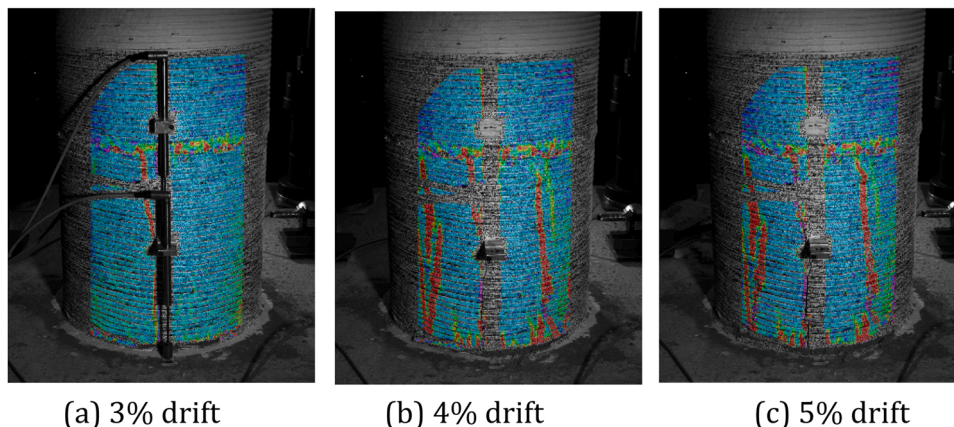


Fig. 8. (a-c) Hoop strain patterns in specimen S1 under compression loading reversals at different drift levels on loading face in push direction.

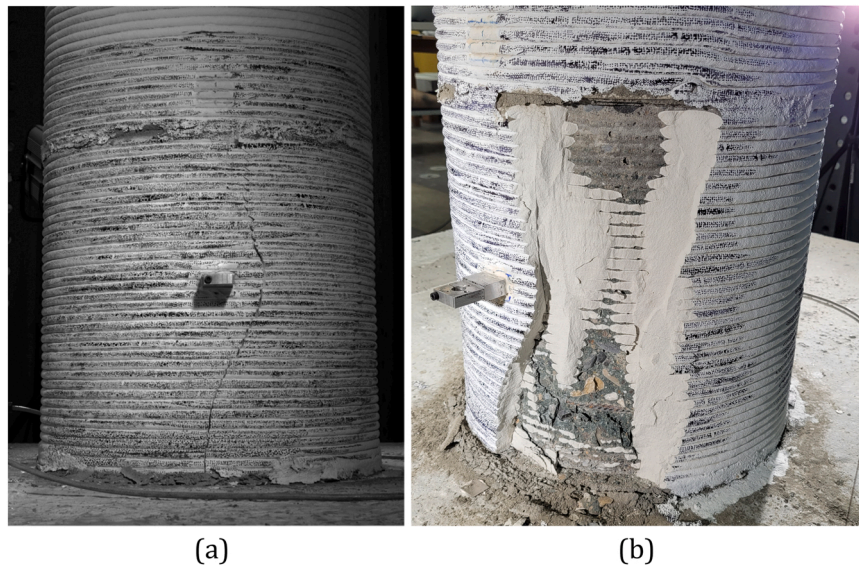


Fig. 9. Failure of 3DPC formwork in Column S1 at 5% drift: (a) cracked formwork immediately prior to separation, (b) close-up showing the diagonal failure planes due to crushing of the unconfined zones to propagate into the 3DPC element.

and around the steel stirrups). Visual observation of the damaged column surface after stopping the test confirmed the presence of fractured concrete wedges between stirrups up to approximately one third of the segment height from the base (Fig. 9(b)). Up to this height, the 3DPC had separated as a single complete piece with cast concrete layers still attached on it, with no visible damage propagating into the 3DPC layer. In the top two thirds of the segment's height, the separated 3DPC surfaces were characterised by diagonal fracture planes that propagated upwards from the crushed concrete core and downwards from the Segment 1-to-Segment 2 joint, due to the high compressive load acting on the formwork. It should be noted that the compressive stresses acting on the 3DPC formwork at high drifts were likely magnified also due to the stress redistribution from the already softening (crushing) cast concrete core at the base of the Segment 1, and the high bearing stresses acting on the top surface of the 3DPC formwork from the rocking Segment 2.

The 3DPC formwork maintained bond with the substrate concrete up until crushing initiation and the fractured pieces confirmed the good interlayer bonding between the deposited 3DPC filaments. No visible interfaces were observed, whereas failure planes propagated in 3DPC diagonally, as they would in cast homogeneous materials. Overall, the 3DPC formwork exhibited good damage tolerance and maintained its integrity until ultimate failure of column S1; total separation took place at 5% drift and only after a significant reduction in the column's lateral load capacity (approximately 40%). Nonetheless, the initiation of the vertical splitting crack at the onset of the column's lateral failure served as additional visual warning for the approaching collapse. The desirable prevention of premature formwork spalling or separation was possible due to the lower modulus of elasticity and the relatively more ductile compressive behaviour of the 3DPC mortar compared to the specified grade of cast concrete (a measured modulus of 28 GPa for 3DPC versus

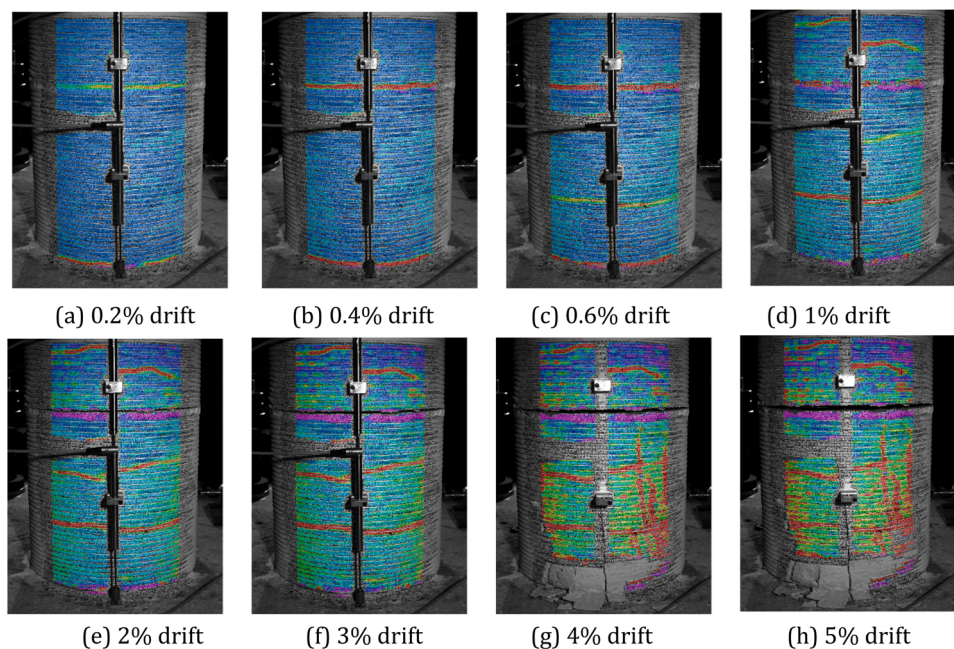


Fig. 10. Axial strain patterns in specimen S2 under tension load reversals at different drift levels on loading face in push direction.

41 GPa for C70/85 grade concrete [70], with similar measured compressive strengths – see Section 2.1). Regardless, future studies should investigate the mechanical compatibility, bond behaviour and integrity between printed and cast concrete in further detail.

The axial strain patterns of Specimen S2 under tension load reversals are shown in Fig. 10. As with Specimen S1, the concentration of horizontal axial strains can be observed at the Footing-to-Segment 1 and Segments 1-to-2 interfaces from small drifts, as shown in Fig. 10 (a) to (d). However, unlike S1, axial strain concentrations also developed in Segment 2 of specimen S2, as shown in Fig. 10 (d) to (h). The results in Fig. 10 (d) to (h) show that the base joint opening in S2, unlike S1, is not very significant. Instead, the joint opening in Specimen S2 was more significant at the Segments 1-to-2 interface. A visible joint opening could be noticed at the interface of segments 1–2 at 2% drift in Fig. 10 (e), which increased with increasing drifts. The greater joint opening at Segments 1-to-2 interface in Specimen S2 was primarily because the bottom face of Segment 2 was pre-cracked at the location of corrugated ducts before assembling owing to manufacturing inconsistencies. This behavior is discussed in more detail in the upcoming sections.

The evolution of hoop strains during compression load reversals in Specimen S2 is shown in Fig. 11 for drifts from 3% to 5%. The results show that large vertical hoop strains developed in Segment 1 of Specimen S2 at 3% drift, resulting in the vertical splitting of the Segment 1 formwork at 4% drift. The vertical splitting cracks in the 3DPC formwork were wider and extended to the full height of Segment 1 in Specimen S2, in contrast to Specimen S1. The location of the vertical splitting crack in both columns was the same, i.e. at the extreme fiber of the cross-section. Unlike specimen S1, separation of the printed and cast concrete was not observed in specimen S2, although some minor spalling of 3DPC formwork was observed at 4% and 5% drift levels (Fig. 11 (b,c)).

Comparison of Figs. 7, 8, 10, and 11 show that the 3DPC formwork of Specimen S2 experienced greater damage than S1, in terms of cracking, spalling, and vertical splitting. This is mainly due to two reasons: i) the limited opening of the base joint at the Footing-to-Segment 1 interface in S2 compared to S1 due to the presence of double amount of ED steel rebars, which provided a greater restraint to the base joint against the opening and prevented the rocking behavior, ii) the higher lateral loads resisted by S2. This essentially implies that the amount of ED rebars should be kept low for better damage control of the proposed columns.

No horizontal slippage was observed across the segment joints in both columns because the shear resistance across the segment joints was quite high compared to the shear demand. The shear resistance across the segment joints depends on the total axial load on the column and the amount of ED rebars, and is given by Eq. 1 [71]. The ratio of the shear demand to shear resistance across the segment joints was 0.11 and 0.1, for columns S1 and S2, respectively.

$$V_n = A_{ED}f_y + 0.75(P_p + P_G) \quad (1)$$

Where, V_n =shear capacity, A_{ED} =total area of ED rebars, P_p =prestressing load, P_G =gravity load.

3.3. Hysteretic force-displacement behavior

Fig. 12 shows the force-displacement hysteresis of the columns with the peak load capacity and lateral load failure points highlighted. Lateral load failure is defined as the point corresponding to a 20% reduction in the lateral strength of the columns. The results show that the lateral load capacity of Specimen S2 was 15% higher than S1. This was mainly due to the higher $\frac{P_{ED}}{P_{SMA}}$ ratio (i.e. 0.6 compared to 0.3) in S2. Note that the additional ED steel rebars were provided at the neutral axis depth in Specimen S2, as shown in Fig. 1(b), therefore the increase in lateral strength on doubling the $\frac{P_{ED}}{P_{SMA}}$ ratio was not very significant. The greater damage observed in S2 as discussed in the previous section, can be primarily attributed to its higher moment capacity owing to the double amount of ED rebars, which resulted in higher ultimate lateral load, and hence higher stresses/strains on the column cross-section compared to S1, and consequently more damage to the concrete. The hysteresis of specimen S1 can generally be observed to be narrower than S2, especially at large drifts, which is indicative of lower energy dissipation. In addition, the pinching effect in the hysteresis seems to be more pronounced for specimen S1, which has a smaller $\frac{P_{ED}}{P_{SMA}}$ ratio. Table 3 summarizes the load and drift capacity of the column at the peak and lateral load failure points. The results show that both columns reached the peak load capacity in the push and pull directions at approximately 2% drift. However, the lateral load failure of Specimen S2 occurred earlier than that of S1, i.e. at 3% and – 3.5% drifts in the push and pull directions, compared to +4% and – 3.9% drifts, respectively for S1. The accelerated strength degradation of Specimen S2 is mainly because it resisted higher loads compared to S1, resulting in greater damage to the concrete. The average strength degradation of specimen S1 at 4% drift was 26.5% compared to 33.3% degradation for S2. The relatively less steep strength degradation of S1 indicates that it exhibited better low-damage characteristics than S2. The peak strength degradation of both columns was less than 50% at 5% drift, indicating that the columns could possibly withstand even higher drifts. The main reason for the accelerated degradation in the lateral load capacity of the column with increasing drifts was the lack of sufficient longitudinal rebars on the loading faces. Both columns were provided with only one ED rebar on each loading face, as shown in Fig. 1(a) and (b). Consequently, the concrete on each loading face experienced higher stresses/strains and corresponding damage, resulting in accelerated degradation of lateral load capacity. This conclusion is confirmed by another recent experimental study carried out by the authors [72], where a similar accelerated degradation in lateral load capacity was observed when only one rebar was provided at each loading face of the column. On the other hand, for the same column configuration, the degradation in load capacity reduced

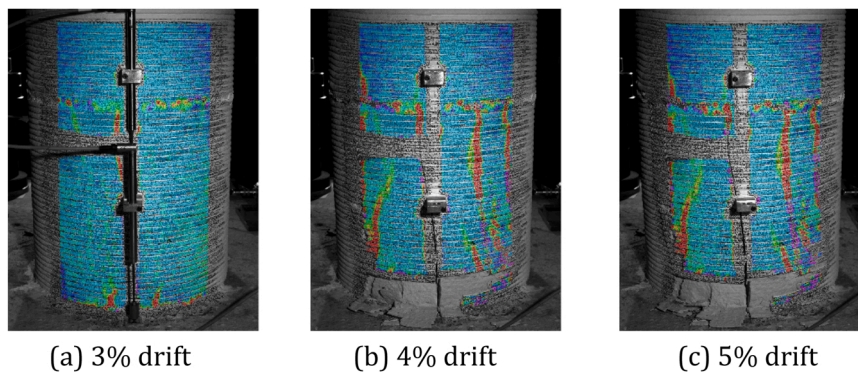


Fig. 11. Hoop strain patterns in specimen S2 under compression load reversals at different drift levels on loading face in push direction.

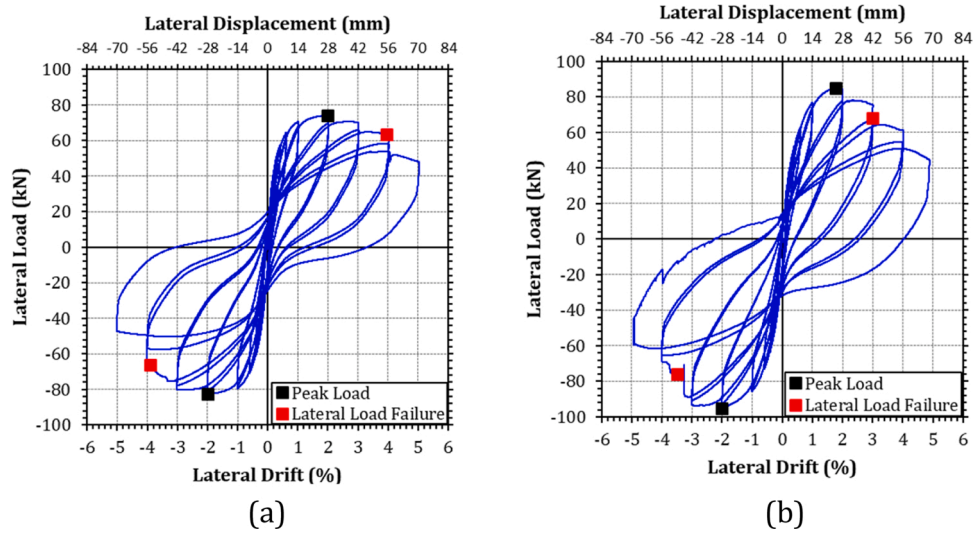


Fig. 12. Force-displacement hysteresis; a) S1; b) S2.

Table 3

Load capacity and drifts at different limit states.

No.	Load Capacity (kN) at				Drift (%) at			
	Peak		Lateral Failure		Peak		Lateral Failure	
	Push	Pull	Push	Pull	Push	Pull	Push	Pull
S1	+ 74	-83	+ 59	-66	+ 2	-2	+ 4	-3.9
S2	+ 85	-95	+ 66	-76	+ 1.77	-2	+ 3	-3.5

significantly when multiple rebars were provided on the loading faces, which allowed the reduction of stresses/strains on the concrete.

The proposed column system is currently recommended to be used in low to moderate seismic regions. This conservative recommendation has been made considering that the columns in this study were subjected to a maximum drift of 5%. However, in high seismic regions, drift demands $\geq 5\%$ are also possible [73]. Furthermore, the lateral loading protocol in the current study was unidirectional and past studies have shown a significant reduction in the collapse drift capacity of the column under multidirectional earthquake actions [74–76] as compared to unidirectional earthquake loading [77]. The performance of the proposed

column system should be investigated under multidirectional earthquake actions before use in high seismic regions.

3.4. Joint opening

The evolution of joint opening between the Footing and Segment 1 and Segments 1 and 2 on the east and west sides of the columns is shown in Fig. 13. The results are shown up to a lateral drift of 3%, as LVDTs were removed for higher drift excursions to protect them from damage. Fig. 13 (a) shows that most of the joint opening occurred between the Footing and Segment 1 in Specimen S1, and very limited opening occurred between Segment 1 and 2 on both the east and west sides of the column. The opening at both joints was symmetrical on both sides. The results indicate that the joint opening between the footing and Segment 1 showed a fourfold increase, with an increase in lateral drift from 1% to 3%, while the joint opening between Segments 1 and 2 showed more than a twofold increase with an increase in drift from 1% to 3%.

In the case of Specimen S2, the joint opening behavior at the same locations was highly asymmetric on the east and west sides, as shown in Fig. 13 (b). The first aspect of asymmetry was that the joint opening between the footing and Segment 1 was significantly larger on the east

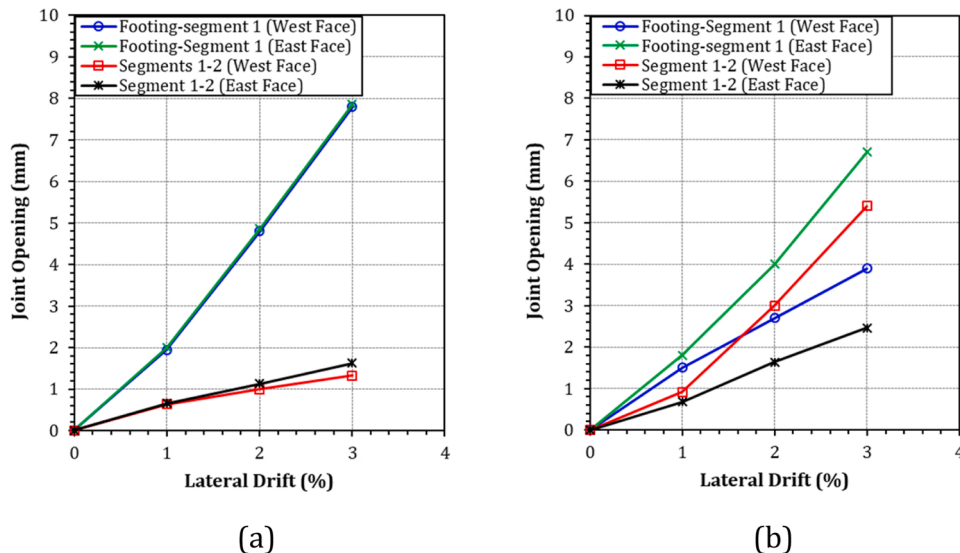


Fig. 13. Joint opening at the Footing-to-Segment 1 and Segments 1-to-2 interfaces; a) S1; b) S2.

side than on the west side of the column. As such, the opening between the footing and Segment 1 increased 3.7 times on the east side and 2.6 times on the west side as the lateral drift increased from 1% to 3%. The second aspect of asymmetry was that on the west side of the column, the joint opening between Segments 1 and 2 became larger than that between the footing and Segment 1 for drifts $\geq 2\%$. In contrast, on the east face, the joint opening between the footing and Segment 1 remained larger than the opening between Segments 1 and 2 for all drift levels. The results show that the joint opening between Segments 1 and 2 showed a 6-fold increase on the west side and a 3.6-fold increase on the east side with an increase in lateral drift from 1% to 3%.

The larger joint opening between Segments 1 and 2 on the west face of specimen S2 is likely attributed to pre-cracking on the underside of Segment 2 before assembling. This crack originated from the base of the corrugated duct and extended diagonally through the cast concrete infill towards the edge of the 3DPC segment. As a result of initial pre-cracking, this joint proved to be a weaker connection, with most of the opening concentrated there. It should be noted that, typically, as the amount of ED steel rebars increase in segmental columns, the opening at the upper joints increases but remains smaller than the opening between the footing and Segment 1 [78]. A similar behavior would have been shown by the columns considered in this study if there was no initial pre-cracking from manufacturing at the Segment 1-to-2 interface in Specimen S2.

3.5. Residual drifts

The residual drifts of the columns in the push and pull loading directions at different target drifts are shown in Fig. 14. The residual drift was determined from the force-displacement hysteresis of each cycle when the lateral load on the column reached zero during unloading. The residual drift limit, which corresponds to a compromise in the functionality of the bridge, has been chosen as 1% following the recommendations of previous studies [79,80].

The results in Fig. 14 indicate that the residual drifts of Specimen S1 were similar in the push and pull directions. The column was able to maintain a residual drift of $\leq 1.0\%$ up to a target drift level of 4% in the push direction and 3.5% in the pull direction. On the other hand, Specimen S2 showed a significant asymmetry in the residual drifts in the push and pull directions. It can be seen that the residual drifts in the push direction of Specimen S2 were approximately half of those observed in

the pull direction. The column was able to maintain a residual drift of 1% up to a target drift level of 2.8% in the push direction and 4% in the pull direction. Moreover, the average residual drifts in the push and pull direction of specimen S2 were higher than S1 owing to the higher $\frac{P_{ED}}{P_{SMA}}$ ratio. The asymmetry of the residual drifts in specimen S2 could be attributed to the asymmetry of the joint opening on the east and west sides of the column, as discussed previously. The smaller residual drifts in the push direction result from a larger opening between the footing and Segment 1 on the east face, as shown in Fig. 13 (b), thereby facilitating the rocking behavior of the column. Conversely, the smaller joint opening between the footing and Segment 1 on the west face resulted in larger residual drifts in the pull direction owing to limited rocking.

The effect of the repetition of loading cycles on the average residual drift of specimens S1 and S2 is shown in Fig. 15. It can be seen that the residual drift in both cycles was similar up to the 2% drift level. The residual drift in the second cycle became slightly greater than the first cycle at 3% drift and the difference between the residual drifts of the two cycles increased further at 4% drift. The increase in residual drifts with loading cycle repetition was mainly due to the accumulation of permanent strains in Fe-SMA and ED steel rebars with each cycle. The figure also shows that the average residual drift of both columns was similar up to 2% drift. However, at 3% and 4% drift levels, the average residual drift of specimen S2 in the second cycle was 33% and 23% greater than S1, mainly due to the higher reinforcement ratio.

The Fe-SMA rebars experience prestress loss under cyclic loading after activation. To elaborate this aspect, the monotonic stress-strain behavior of Fe-SMA rebar and the behavior on initial prestraining and subsequent unloading is shown in Fig. 16. It was concluded in [48] that the cyclic strain amplitude corresponding to the complete loss of prestress of Fe-SMA is equal to the recovered strains on unloading of the Fe-SMA rebar after initial prestraining, as the material behaves like a viscoelastic spring within this strain range without accumulation of any residual strains. This strain range was reported to be about 0.4–0.5% for Fe-SMA with an initial prestrain of 4%, as shown in Fig. 16 (b). The stress amplitude corresponding to this strain range was found to be about 200 MPa. This means that Fe-SMA rebars can partially retain the initial prestress as long as the stress due to cyclic loading is below 200 MPa. The study also showed that the strain range within which Fe-SMA rebar partially retains initial prestress can be increased to about 1.25% by heat treatment at 750 °C for 6 h.

The prestress loss behavior of Fe-SMA is in contrast with the conventional tendons, which have a high yield strength and tend to remain elastic until high column drifts. This may appear as a drawback of Fe-SMA reinforced columns. However, it is important to consider that conventional tendons, due to their predominantly elastic behaviour, do not contribute significantly to the energy dissipation of the column. Therefore, post-tensioned columns with tendons need additional measures to meet the energy dissipation requirements at high drift demands.

In contrast, once the prestress is lost, the high ductility of Fe-SMA rebars (refer Fig. 16a) enables them to contribute to the energy dissipation capacity of the columns. This allows Fe-SMA rebars to contribute both to self-centering and energy dissipation capacity, whereas conventional tendons primarily contribute to self-centering of the columns. Consequently, what may seem as a drawback—prestress loss in Fe-SMA reinforced columns—can actually be viewed as an advantage, as Fe-SMA reinforced columns do not require additional measures for enhancing the energy dissipation capacity at high drift demands. Nonetheless, it is worth noting that this loss of prestress in Fe-SMA rebars would typically happen in the outermost rebars at the loading faces of the columns. In contrast, Fe-SMA rebars located around neutral axis will experience less strains, and resultantly lose less prestress. As a result, these rebars continue to contribute to self-centering even at high drifts, while the outermost rebars contribute to the energy dissipation after losing the prestress. This was shown in a previous study [72] conducted by the authors (in which strain gauges were installed on the Fe-SMA rebars)

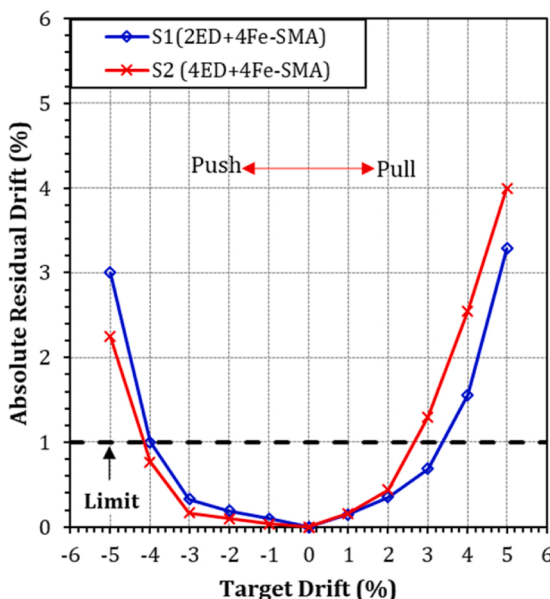


Fig. 14. Residual drift of the columns at various target drifts.

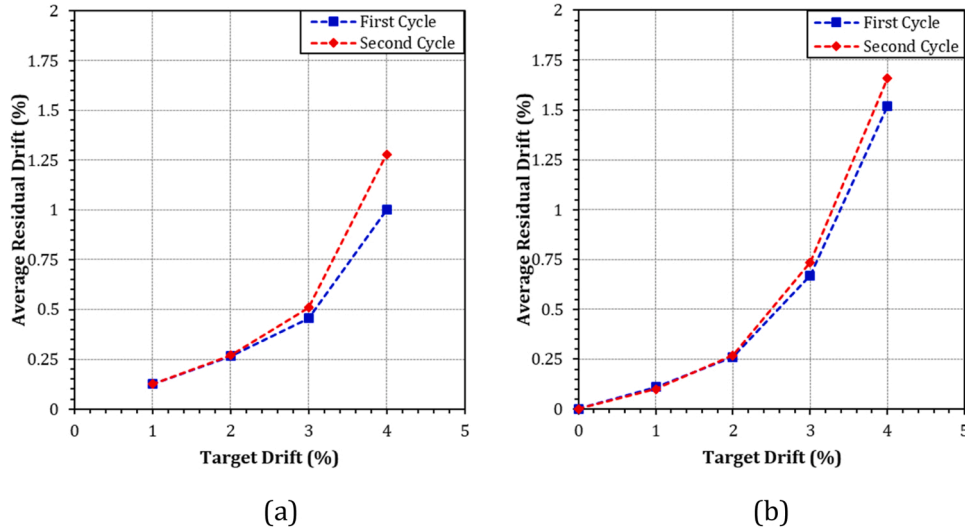


Fig. 15. Effect of repetitive loading cycles on the residual drift of columns: a) S1; b) S2.

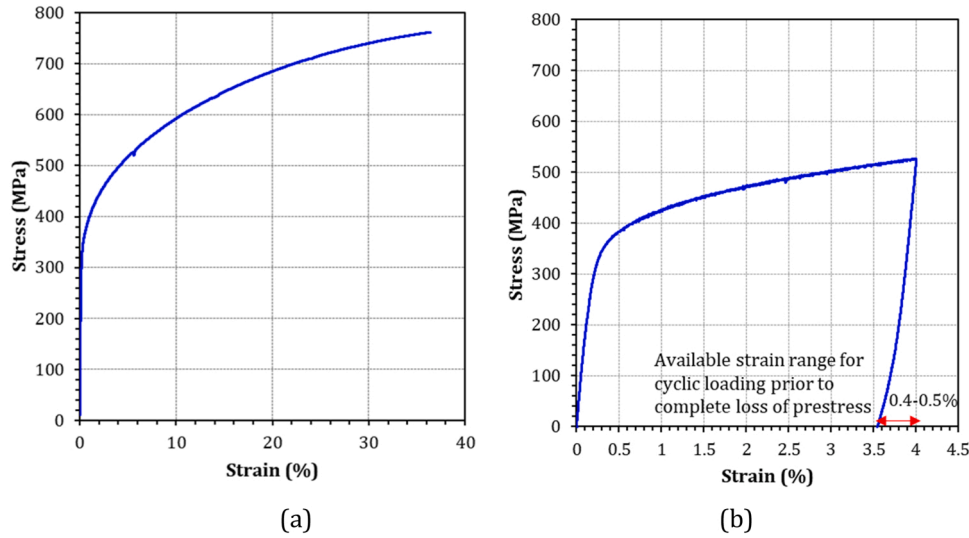


Fig. 16. (a) Monotonic stress-strain behaviour of Fe-SMA rebars; (b) available strain range for cyclic loading prior to complete loss of prestress for Fe-SMA with 4% initial prestrain (adapted from [48])

where the outermost Fe-SMA rebars reached 0.4–0.5% strain range when the column drift was between 2 to 3%. On the other hand, Fe-SMA rebars located at the neutral axis remained below this strain range until 5% drift and still contributed to self-centering. Considering this, the Fe-SMA rebars were positioned at the center of the cross-section instead of the extreme loading faces in the current study. However, since the strain gauges could not be installed on the rebars owing to the issues related to the column fabrication, the strains in the rebars at different drift levels are not known. It is recommended that future studies on the proposed column system should use load cells or strain gauges to determine the drift levels corresponding to the complete loss of prestress in Fe-SMA rebars.

3.6. Energy dissipation

The hysteretic energy dissipation was determined by calculating the area under the force-displacement hysteretic curve in each load cycle. The total hysteretic energy dissipation, which represents the cumulative energy dissipated in all load cycles is shown in Fig. 17 (a). The results show that the total hysteretic energy dissipation of specimen S2 was

only 7% greater than that of S1. The plot of the hysteretic energy dissipation in the second cycle of each drift excursion is shown in Fig. 17 (b). It shows that the energy dissipation of both columns was more or less the same up to 2% drift. However, from 3% drift, the energy dissipation of specimen S2 was higher than that of S1 and the difference between the energy dissipation of the two columns increased with each subsequent drift excursion. The smaller increase in energy dissipation despite a higher $\frac{P_{ED}}{P_{SMA}}$ in S2 is because the additional ED steel rebars were placed at the neutral axis depth. As a result, these rebars experienced relatively smaller strains, resulting in little contribution to the hysteretic energy dissipation of the column at high drifts.

3.7. Stiffness degradation

The stiffness of the columns was determined from the force-displacement hysteresis in each load cycle using Eq. (2).

$$k_i = \frac{|+F_i| + |-F_i|}{|+\Delta_i| + |-\Delta_i|} \quad (2)$$

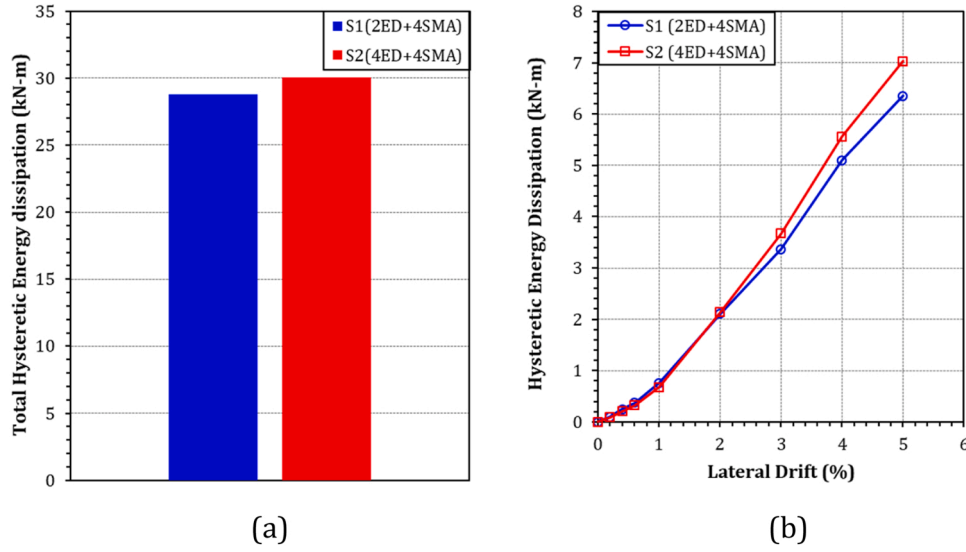


Fig. 17. Energy dissipation behavior of the columns: a) total hysteretic energy dissipation; b) hysteretic energy dissipation in each loading cycle.

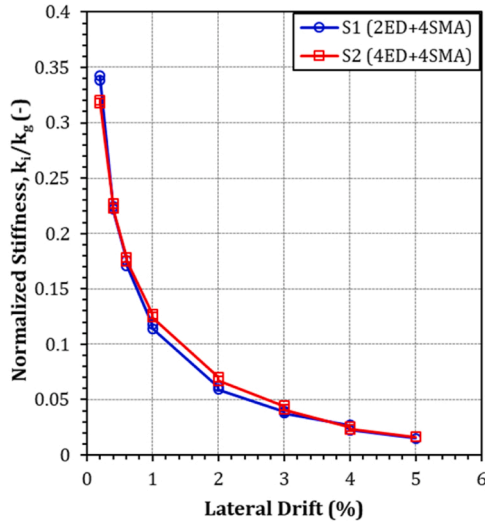


Fig. 18. Normalized stiffness of the columns with increasing lateral drifts.

Where $+F_i$ = lateral force in pull direction in each cycle; $-F_i$ = lateral force in push direction in each cycle; $+\Delta_i$ = displacement in pull direction in each cycle; $-\Delta_i$ = displacement in push direction in each cycle.

The stiffness in each load cycle (k_i) was normalized to the gross stiffness (k_g) of the columns. The gross stiffness of the column was determined based on the uncracked section properties. The results of the normalized stiffness with increasing lateral drift of the column are shown in Fig. 18. It can be seen that the stiffness degradation behavior of both columns was generally the same. The initial stiffness of specimen S2 was slightly lower than S1 due to the asymmetry of its load capacity in the push and pull loading directions owing to pre-cracking. However, at higher drifts, particularly from 1% to 3%, specimen S2 showed a higher stiffness than S1 due to its higher load capacity. The stiffness degradation plot shows a rapid degradation of the initial stiffness of the columns up to 1% drift, with the columns losing approximately 60% of their initial stiffness. After that, the stiffness degradation was more gradual. The remaining stiffness of the columns at the end of the experiment was only 5% of the initial stiffness.

The effective stiffness of the columns was calculated from the average force-displacement backbone curve (average of push and pull directions) based on the gradient of a line from the origin to the point

Table 4

Effective moment of inertia of the columns.

No.	Effective Moment of Inertia I_{eff}			
	Experimental	Paulay and Priestley [82]	Haselton et al. [83]	ASCE/SEI 41-17 [84]
S1	$0.19I_g$	$0.29I_g$	$0.28I_g$	$0.29I_g$
S2	$0.15I_g$	$0.29I_g$	$0.28I_g$	$0.29I_g$

where the column yields. The yield load of the column was determined from the force-displacement hysteresis using the reduced stiffness equivalent elastoplastic yield method [81]. In this method, the yield point is calculated based on the intersection of a line that passes from $0.75F_{max}$ and the horizontal line drawn from F_{max} . The effective stiffness was used to determine the effective moment of inertia of the columns. Table 4 shows the effective moment of inertia of the tested columns and compares it with existing models for conventional monolithic columns from Paulay and Priestley [82], Haselton et al. [83] and ASCE 41–17 [84]. The expressions for these models are as follows:

Paulay and Priestley [82]:

$$\frac{I_{eff}}{I_g} = \frac{100}{f_y} + n \quad (3)$$

Haselton et al. [83]:

$$\frac{I_{eff}}{I_g} = -0.07 + 0.59n + 0.07 \frac{L}{h} \quad (4)$$

ASCE/SEI 41–17 [84]:

$$\frac{I_{eff}}{I_g} = 0.7 \text{ for } n \geq 0.5 \quad (5)$$

$$\frac{I_{eff}}{I_g} = 0.3 \text{ for } n \leq 0.1 \quad (6)$$

Where I_{eff} = effective moment of inertia; I_g = gross moment of inertia; n = total axial load ratio including gravity and prestress; f_y = yield strength of longitudinal steel; L = shear span length; h = depth of cross-section.

The results in Table 4 show that the effective moment of inertia of specimen S2 was 20% lower than that of S1, despite the higher number of ED steel rebars, mainly due to the pre-cracking of Segment 2 of S2 resulting from manufacturing inconsistencies. The comparison of the

experimental moment of inertia with that of existing predictive models for conventional monolithic columns shows that the effective moment of inertia of segmental columns is significantly less than that expected for monolithic columns. This finding is consistent with previous studies on post-tensioned segmental columns where a lower effective moment of inertia in the range of $0.16\text{--}0.17I_g$ was obtained [29]. The lower effective moment of inertia of prestressed segmental columns is mainly due to the joint opening, which introduces flexibility and reduces the overall stiffness of the column.

3.8. Axial displacement-lateral drift behavior

The axial displacement behavior of specimens S1 and S2 with increasing lateral drifts is shown in Fig. 19. The columns experienced maximum shortening at the origin (zero drift) and maximum elongation at the peak drifts in each load cycle. The maximum shortening of both columns was about 0.6 mm. Specimen S1 experienced a maximum elongation in the range of 3.25 to 3.8 mm at 5% drift. In contrast, specimen S2 showed a highly asymmetric elongation behavior in the push and pull directions. Notably, the axial elongation during pulling was significantly lower than during pushing for each displacement excursion. This behavior is due to the asymmetric joint opening on the east and west sides of the column. The lower axial elongation during pulling can be attributed to the relatively small opening at the Footing-to-Segment 1 joint on the west side of the column, as shown in Fig. 13 (b). Conversely, the axial elongation during pushing was greater due to the larger joint opening on the east side of the column, as illustrated in Fig. 13 (b). The maximum elongation of specimen S2 was 2.5 mm during pulling and 3.8 mm during pushing at 5% drift.

4. Conclusions

This study proposed a novel prefabrication concept for the accelerated construction of segmental bridge columns by integrating digital fabrication technology with an advanced SMA-based prestressing technique. The feasibility of the proposed concept was evaluated through large-scale experiments on columns under combined gravity and quasi-static lateral loading. Based on the results of the experiments, the following conclusions can be drawn:

1. The proposed prefabrication concept for segmental bridge columns, consisting of permanent 3DPC formwork for column segment fabrication and prestressing of the column assembly using Fe-SMA rebars,

is feasible, particularly for application in low to moderate seismic regions.

2. The proposed segmental column system exhibited a controlled rocking behavior under lateral loading, with a joint opening between the footing and Segment 1 and Segments 1 and 2. The prestressing with Fe-SMA rebars enabled a low-damage performance and as a result, the columns were able to withstand 5% drift without collapsing. Furthermore, the strength degradation of the columns was less than 50% up to 5% drift, indicating some reserve capacity for higher drifts.
3. The 3DPC formwork showed no significant damage up to 3% drift and remained attached to the cast concrete substrate throughout the experiment. The formwork of the bottommost column segment experienced vertical splitting in hoop tension at 4% and 5% drift levels due to high axial compressive stresses but remained bonded to the concrete core until the end of the lateral loading test. The remaining three segments showed little to no damage.
4. The columns showed a strong self-centering behavior up to a drift of 3%, with an average residual drift less than 1%. With the further increase in drift, the residual drift also increased due to the loss of prestress in Fe-SMA rebars and accumulation of residual strains in ED rebars. Among the two alternative designs considered, the column with $\frac{P_{ED}}{P_{SMA}} = 0.3$ showed 20–30% lower residual drifts compared to the column with $\frac{P_{ED}}{P_{SMA}} = 0.6$.
5. The column with $\frac{P_{ED}}{P_{SMA}} = 0.6$ showed 15% higher lateral strength and 7% higher energy dissipation than the column with $\frac{P_{ED}}{P_{SMA}} = 0.3$. The relatively small increase in energy dissipation and lateral strength despite doubling the number of ED steel rebars was because the additional rebars were placed at the neutral axis depth. These rebars experienced relatively smaller strains, resulting in a little contribution to the hysteretic energy of the column at high drifts. Overall, the column with $\frac{P_{ED}}{P_{SMA}} = 0.3$ exhibited better low-damage characteristics due to the greater foundation-Segment 1 joint opening, resulting in less damage to the 3DPC formwork.

The results of this study showcase the feasibility of the proposed concept of segmental prefabrication, consisting of 3DPC formwork and prestressed Fe-SMA rebars, for bridge columns. It is worth noting that, among other benefits, the proposed fabrication technique combines the use of 3DPC with conventional concrete containing large aggregates, thus helping to reduce the high cement content and the associated CO_2

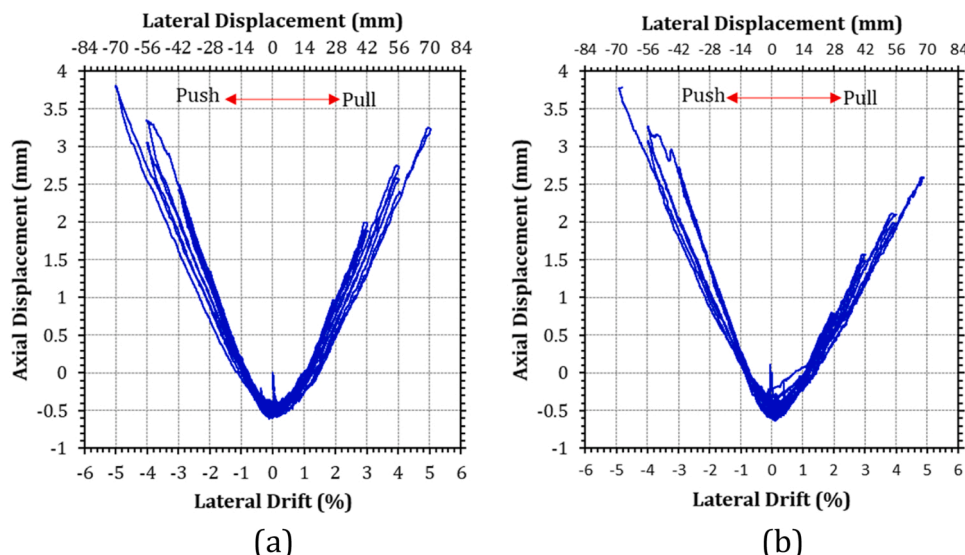


Fig. 19. Axial displacement-lateral drift behavior of the columns: a) S1; b) S2.

emissions that are currently inherent in loadbearing structures that are purely based on 3DPC.

From a structural point of view, future studies should investigate the effect of design parameters such as the amount of initial prestressing, the axial load ratio, and the loading history on the seismic performance of the proposed column system. It is also recommended that future studies should investigate the bond strength between printed and cast concrete under tension, shear and shear-compression loading using small-scale experiments to better understand the mechanism of bond between the printed and cast concrete. The durability performance including weathering resistance of the 3DPC shell should also be investigated in the future. Given the positive results of the feasibility study, future work could also investigate optimized geometries for the formwork shells that can be fabricated efficiently (without any cost increase) through 3D printing. This could include overall shape optimization of the 3DPC formwork shells, geometric variation between the segments, and the integration of additional functionality including printing of formwork shells with integrated ducts.

CRedit authorship contribution statement

Shahverdi Moslem: Conceptualization, Funding acquisition, Methodology, Supervision, Writing – review & editing. **Triantafyllidis Zafiris:** Conceptualization, Formal analysis, Investigation, Methodology, Writing – review & editing. **Anton Ana:** Conceptualization, Writing – review & editing. **Dillenburger Benjamin:** Conceptualization, Funding acquisition, Supervision, Writing – review & editing. **Raza Saim:** Conceptualization, Formal analysis, Investigation, Methodology, Writing – original draft.

Declaration of Competing Interest

The authors declare that they have no known competing financial interests or personal relationships that could have appeared to influence the work reported in this paper.

Data Availability

Data will be made available on request.

Acknowledgments

The authors would like to acknowledge Dr. Mateusz Wyrzykowski and Dr. Volha Semianiuk for their scientific support and the staff of the Empa Structural Engineering Laboratory for their technical support, in particular Mr. Robert Widmann and Mr. Werner Studer. The authors are also grateful to the industrial partner, re-fer AG, for providing the materials and technical support with prestress activation. The financial support of the Department of Engineering Sciences at Empa and the Institute of Technology in Architecture at ETH Zurich is also gratefully acknowledged.

References

- [1] Khoshnevis B. Automated construction by contour crafting—related robotics and information technologies. *Autom Constr* 2004;13(1):5–19. <https://doi.org/10.1016/j.autcon.2003.08.012>.
- [2] Gosselin C, Duballet R, Roux P, Gaudillière N, Dirrenberger J, Morel P. Large-scale 3D printing of ultra-high performance concrete – a new processing route for architects and builders. *Mater Des* 2016;100:102–9. <https://doi.org/10.1016/j.matdes.2016.03.097>.
- [3] Johnston DW. Design and construction of concrete formwork. In: Nawy Edward G, editor. *Concrete construction engineering handbook*. New Jersey, USA: Boca Raton: CRC Press; 2008. p. 7.1–7.49.
- [4] Dong YH, Jaillon L, Chu P, Poon CS. Comparing carbon emissions of precast and cast-in-situ construction methods – a case study of high-rise private building. *Constr Build Mater* 2015;99:39–53. <https://doi.org/10.1016/j.conbuildmat.2015.08.145>.
- [5] Zhu B, Nematollahi B, Pan J, Zhang Y, Zhou Z, Zhang Y. 3D concrete printing of permanent formwork for concrete column construction. *Cem Concr Compos* 2021;121:104039. <https://doi.org/10.1016/j.cemconcomp.2021.104039>.
- [6] Chen Y, Zhang W, Zhang Y, Zhang Y, Liu C, Wang D, et al. 3D Printed concrete with coarse aggregates: built-in-Stirrup permanent concrete formwork for reinforced columns. *J Build Eng* 2023;70:106362. <https://doi.org/10.1016/j.jobe.2023.106362>.
- [7] Anton A, Reiter L, Wangler T, Frangez V, Flatt RJ, Dillenburger B. A 3D concrete printing prefabrication platform for bespoke columns. *Autom Constr* 2021;122:103467. <https://doi.org/10.1016/j.autcon.2020.103467>.
- [8] Gaudillière, N., Duballet, R., Bouyssou, C., Mallet, A., Roux, P., Zakeri, M., & et al. (2019). Large-Scale Additive Manufacturing of Ultra-High-Performance Concrete of Integrated Formwork for Truss-Shaped Pillars. Paper presented at the Robotic Fabrication in Architecture, Art and Design 2018, Cham.
- [9] Anton, A., Reiter, L., Skevaki, E., Dillenburger, B. (2022). Reinforcement Lattices for 3DCP: A Fabrication Method Based on Ruled Surfaces. In *Structures and Architecture A Viable Urban Perspective?* Taylor & Francis Group. <https://doi.org/10.1201/9781003023555-33>.
- [10] Block, India (2019). World's largest 3D-printed building completes in Dubai. *Dezeen*, December 22nd. (<https://www.dezeen.com/2019/12/22/apis-cor-worlds-largest-3d-printed-building-dubai/>) Accessed 19.06.2023.
- [11] Zhang P, Xu F, Liu Y, Ahmed Sheikh S. Shear behaviour of composite beams with permanent UHPC formwork and high-strength steel rebar. *Constr Build Mater* 2022;352:128951. <https://doi.org/10.1016/j.conbuildmat.2022.128951>.
- [12] Gebhard L, Mata-Falcón J, Anton A, Dillenburger B, Kaufmann W. Structural behaviour of 3D printed concrete beams with various reinforcement strategies. *Eng Struct* 2021;240:112380. <https://doi.org/10.1016/j.engstruct.2021.112380>.
- [13] Gebhard, L., Bischof, P., Anton, A., Mata-Falcón, J., Dillenburger, B., & Kaufmann, W. (2022, 2022/). Pre-installed Reinforcement for 3D Concrete Printing. Paper presented at the Third RILEM International Conference on Concrete and Digital Fabrication, Cham.
- [14] Mata-Falcón J, Bischof P, Huber T, Anton A, Burger J, Ranaudo F, et al. Digitally fabricated ribbed concrete floor slabs: a sustainable solution for construction. *RILEM Tech Lett* 2022;7:68–78. <https://doi.org/10.21809/rilemtechlett.2022.161>.
- [15] Ma G, Buswell R, Leal da Silva WR, Wang L, Xu J, Jones SZ. Technology readiness: a global snapshot of 3D concrete printing and the frontiers for development. *Cem Concr Res* 2022;156:106774. <https://doi.org/10.1016/j.cemconres.2022.106774>.
- [16] International Federation for Structural Concrete (fib), fib Bulletin No. 82: Precast segmental bridges - Guide to good practice. 2017, International Federation for Structural Concrete (fib): Lausanne, Switzerland. p. 183.
- [17] Billington SL, Barnes RW, Breen JE. A precast segmental substructure system for standard bridges. *PCI J* 1999;44(4):56–73. <https://doi.org/10.15554/pci.07011999.56.73>.
- [18] Figg L, Pate WD. Precast concrete segmental bridges - America's beautiful and affordable icons. *PCI J* 2004;49(5):26–38.
- [19] Shahawy MA. NCHRP Synthesis of Highway Practice 324: Prefabricated Bridge Elements and Systems to Limit Traffic Disruption During Construction. Washington, D.C.: Transportation Research Board of the National Academies; 2003.
- [20] Fawaz G, Murcia-Delso J, Bayrak O. Synthesis of Precast Bridge Column Designs. Report FHWA/TX-19/0-6978-1. Center for Transportation. The University of Texas at Austin; 2019.
- [21] Hewes JT, Priestley MN. Seismic design and performance of precast concrete segmental bridge columns. Rep. No. SSRP 2001/25. La Jolla, CA: Univ. of California San Diego; 2002.
- [22] Yamashita R, Sanders DH. Seismic performance of precast unbonded prestressed concrete columns. *Acids Struct J* 2009;106(6):821–30.
- [23] Wang J-C, Ou Y-C, Chang K-C, Lee GC. Large-scale seismic tests of tall concrete bridge columns with precast segmental construction. *Earthq Eng Struct Dyn* 2008;37(12):1449–65. <https://doi.org/10.1002/eqe.824>.
- [24] Ou Y-C, Wang P-H, Tsai M-S, Chang K-C, Lee George C. Large-scale experimental study of precast segmental unbonded posttensioned concrete bridge columns for seismic regions. *J Struct Eng* 2010;136(3):255–64. [https://doi.org/10.1061/\(ASCE\)ST.1943-541X.0000110](https://doi.org/10.1061/(ASCE)ST.1943-541X.0000110).
- [25] Motaref S, Saidi MS, Sanders D. Shake table studies of energy-dissipating segmental bridge columns. *J Bridge Eng* 2014;19(2):186–99. [https://doi.org/10.1061/\(ASCE\)BE.1943-5592.0000518](https://doi.org/10.1061/(ASCE)BE.1943-5592.0000518).
- [26] Li C, Hao H, Zhang X, Bi K. Experimental study of precast segmental columns with unbonded tendons under cyclic loading. *Adv Struct Eng* 2017;21(3):319–34. <https://doi.org/10.1177/1369433217717119>.
- [27] Wang J, Wang Z, Tang Y, Liu T, Zhang J. Cyclic loading test of self-centering precast segmental unbonded posttensioned UHPFRC bridge columns. *Bull Earthq Eng* 2018;16(11):5227–55. <https://doi.org/10.1007/s10518-018-0331-y>.
- [28] Moussa AMA, Fahmy MFM, Wu Z. Innovative resilient system of precast segmental RC hollow bridge columns. *Eng Struct* 2021;229:111555. <https://doi.org/10.1016/j.engstruct.2020.111555>.
- [29] Wang Z, Wang J-Q, Tang Y-C, Liu T-X, Gao Y-F, Zhang J. Seismic behavior of precast segmental UHPC bridge columns with replaceable external cover plates and internal dissipaters. *Eng Struct* 2018;177:540–55. <https://doi.org/10.1016/j.engstruct.2018.10.012>.
- [30] Li C, Bi K, Hao H, Zhang X, Van Tin D. Cyclic test and numerical study of precast segmental concrete columns with BFRP and TEED. *Bull Earthq Eng* 2019;17(6):3475–94. <https://doi.org/10.1007/s10518-019-00597-1>.
- [31] Bu Z-Y, Ou Y-C, Song J-W, Zhang N-S, Lee George C. Cyclic loading test of unbonded and bonded posttensioned precast segmental bridge columns with

- circular section. *J Bridge Eng* 2016;21(2):04015043. [https://doi.org/10.1061/\(ASCE\)BE.1943-5592.0000807](https://doi.org/10.1061/(ASCE)BE.1943-5592.0000807).
- [32] Shahverdi M, Michels J, Czaderski C, Motavalli M. Iron-based shape memory alloy strips for strengthening RC members: material behavior and characterization. *Constr Build Mater* 2018;173:586–99.
- [33] Raza S, Shafei B, Saidi Saïdi M, Motavalli M, Shahverdi M. Shape memory alloy reinforcement for strengthening and self-centering of concrete structures—state of the art. *Constr Build Mater* 2022;324:126628. <https://doi.org/10.1016/j.conbuildmat.2022.126628>.
- [34] Rojob H, El-Hacha R. Self-prestressing using iron-based shape memory alloy for flexural strengthening of reinforced concrete beams. *Acids Struct J* 2017;114(2). <https://doi.org/10.14359/51689455>.
- [35] Michels J, Shahverdi M, Czaderski C. Flexural strengthening of structural concrete with iron-based shape memory alloy strips. *Struct Concr* 2018;19(3):876–91. <https://doi.org/10.1002/suco.201700120>.
- [36] Hong K, Lee S, Yeon Y, Jung K. Flexural response of reinforced concrete beams strengthened with near-surface-mounted Fe-based shape-memory alloy strips. *Int J Concr Struct Mater* 2018;12(1):45. <https://doi.org/10.1186/s40069-018-0279-y>.
- [37] Strieder E, Aigner C, Petauschnig G, Horn S, Marcon M, Schwen M, et al. Strengthening of reinforced concrete beams with externally mounted sequentially activated iron-based shape memory alloys. *Materials* 2019;12(3). <https://doi.org/10.3390/ma12030345>.
- [38] Schranz B, Michels J, Czaderski C, Motavalli M, Vogel T, Shahverdi M. Strengthening and prestressing of bridge decks with ribbed iron-based shape memory alloy bars. *Eng. Struct* 2021;241:112467. <https://doi.org/10.1016/j.engstruct.2021.112467>.
- [39] Schranz B, Wagner P-R, Czaderski C, Shahverdi M. Fibre optic measurements and model uncertainty quantification for Fe-SMA strengthened concrete structures. *Eng Struct* 2022;256:114005. <https://doi.org/10.1016/j.engstruct.2022.114005>.
- [40] Montoya-Coronado LA, Ruiz-Pinilla JG, Ribas C, Cladera A. Experimental study on shear strengthening of shear critical RC beams using iron-based shape memory alloy strips. *Eng Struct* 2019;200:109680. <https://doi.org/10.1016/j.engstruct.2019.109680>.
- [41] Cladera A, Montoya-Coronado LA, Ruiz-Pinilla JG, Ribas C. Shear strengthening of slender reinforced concrete T-shaped beams using iron-based shape memory alloy strips. *Eng Struct* 2020;221:111018. <https://doi.org/10.1016/j.engstruct.2020.111018>.
- [42] Czaderski C, Shahverdi M, Michels J. Iron based shape memory alloys as shear reinforcement for bridge girders. *Constr Build Mater* 2021;274:121793. <https://doi.org/10.1016/j.conbuildmat.2020.121793>.
- [43] Fawaz G, Murcia-Delso J. Bond behavior of iron-based shape memory alloy reinforcing bars embedded in concrete. *Mater Struct* 2020;53(5):114. <https://doi.org/10.1617/s11527-020-01548-y>.
- [44] Schranz B, Czaderski C, Vogel T, Shahverdi M. Bond behaviour of ribbed near-surface-mounted iron-based shape memory alloy bars with short bond lengths. *Mater Des* 2020;191:108647. <https://doi.org/10.1016/j.matdes.2020.108647>.
- [45] Schranz B, Czaderski C, Vogel T, Shahverdi M. Bond investigations of pre-stressed, near-surface-mounted, ribbed memory-steel bars with full bond length. *Mater Des* 2020;196:109145. <https://doi.org/10.1016/j.matdes.2020.109145>.
- [46] Schranz B, Nunes MF, Czaderski C, Shahverdi M. Fibre optic strain measurements for bond modelling of prestressed near-surface-mounted iron-based shape memory alloy bars. *Constr. Build Mater* 2021;288:123102. <https://doi.org/10.1016/j.conbuildmat.2021.123102>.
- [47] Raza S, Michels J, Schranz B, Shahverdi M. Anchorage behavior of Fe-SMA re-bars Post-Installed into concrete. *Eng Struct* 2022;272:114960. <https://doi.org/10.1016/j.engstruct.2022.114960>.
- [48] Raza S, Michels J, Shahverdi M. Uniaxial behavior of pre-stressed iron-based shape memory alloy rebars under cyclic loading reversals. *Constr Build Mater* 2022;326:126900. <https://doi.org/10.1016/j.conbuildmat.2022.126900>.
- [49] Yang Y, Leinenbach C, Shahverdi M. Simulation and experimental characterization of VC precipitation and recovery stress formation in an FeMnSi-based shape memory alloy. *J Alloy Compd* 2023;940:168856.
- [50] Yang Y, Breveglieri M, Shahverdi M. Effect of phase changes on the axial modulus of an FeMnSi-shape memory alloy. *Materials* 2021;14(17). <https://doi.org/10.3390/ma14174815>.
- [51] Yang Y, Arabi-Hashemi A, Leinenbach C, Shahverdi M. Influence of thermal treatment conditions on recovery stress formation in an FeMnSi-SMA. *Mater Sci Eng: A* 2021;802:140694.
- [52] Abouali S, Shahverdi M, Ghassemieh M, Motavalli M. Nonlinear simulation of reinforced concrete beams retrofitted by near-surface mounted iron-based shape memory alloys. *Eng Struct* 2019;187:133–48. <https://doi.org/10.1016/j.engstruct.2019.02.060>.
- [53] Dolatabadi N, Shahverdi M, Ghassemieh M, Motavalli M. RC structures strengthened by an iron-based shape memory alloy embedded in a shotcrete layer—nonlinear finite element modeling. *Materials* 2020;13(23). <https://doi.org/10.3390/ma13235504>.
- [54] Rezapour M, Ghassemieh M, Motavalli M, Shahverdi M. Numerical modeling of unreinforced masonry walls strengthened with Fe-based shape memory alloy strips (MDPI AG) *Materials* 2021;14(11):2961. <https://doi.org/10.3390/ma14112961>.
- [55] Cruz Noguez CA, Saidi MS. Performance of advanced materials during earthquake loading tests of a bridge system. *J Struct Eng (U S)* 2013;139(1):144–54. [https://doi.org/10.1061/\(ASCE\)ST.1943-541X.0000611](https://doi.org/10.1061/(ASCE)ST.1943-541X.0000611).
- [56] Saidi MS, O'Brien M, Mahmoud SZ. Cyclic response of concrete bridge columns using superelastic nitinol and bendable concrete. *Acids Struct J* 2009;106(1):69–77.
- [57] Chen Z-P, Zhu S. Development of a novel shape memory alloy-based self-centering precast segmental concrete column. *Struct Control Health Monit* 2022;29(12):e3099. <https://doi.org/10.1002/stc.3099>.
- [58] Zheng Y, Fang C, Liang D, Sun R. An innovative seismic-resilient bridge with shape memory alloy-washer-based footing rocking RC piers. *J Intell Mater Syst Struct* 2020;32(5):549–67. <https://doi.org/10.1177/1045389X20963167>.
- [59] Fang C, Liang D, Zheng Y, Yam MCH, Sun R. Rocking bridge piers equipped with shape memory alloy (SMA) washer springs. *Eng Struct* 2020;214:110651. <https://doi.org/10.1016/j.engstruct.2020.110651>.
- [60] Fang C. SMAs for infrastructures in seismic zones: a critical review of latest trends and future needs. *J Build Eng* 2022;57:104918. <https://doi.org/10.1016/j.jobbe.2022.104918>.
- [61] Buswell RA, da Silva WRL, Bos FP, Schipper HR, Lowke D, Hack N, et al. A process classification framework for defining and describing Digital Fabrication with Concrete. *Cem Concr Res* 2020;134:106068. <https://doi.org/10.1016/j.cemconres.2020.106068>.
- [62] Roussel N, Lowke (Eds.), Digital Fabrication With Cement-based Materials: State-of-the-art Report of the RILEM TC 276-DFC, 978-3-030-90535-4, Springer International Publishing (2022), pp. 99–136, 10.1007/978-3-030-90535-4_4.
- [63] Zhang Q, Alam MS. State-of-the-art review of seismic-resistant precast bridge columns. *J Bridge Eng* 2020;25(10):03120001. [https://doi.org/10.1061/\(ASCE\)BE.1943-5592.0001620](https://doi.org/10.1061/(ASCE)BE.1943-5592.0001620).
- [64] Flatt RJ, Wangler T. On sustainability and digital fabrication with concrete. *Cem Concr Res* 2022;158:106837. <https://doi.org/10.1016/j.cemconres.2022.106837>.
- [65] Sika Schweiz A.G. Technical Data Sheet SikaGrout-311 (2013).
- [66] EN 1998-2. Eurocode 8: Design of structures for earthquake resistance – Part 2: Bridges 2005.
- [67] BSI, BS EN 1991-1-2:2002. Eurocode 1: Actions on structures — Part 1-2: General actions - actions on structures exposed to fire. London, United Kingdom: British Standards International; 2002.
- [68] BSI, BS EN 1992-1-2:2004. Eurocode 2: design of concrete structures — part 1-2: general rules — structural fire design. London, United Kingdom: British Standards International; 2004.
- [69] Melo J, Triantafyllidis Z, Rush D, Bisby L, Rossetto T, Arède A, et al. Cyclic behaviour of as-built and strengthened existing reinforced concrete columns previously damaged by fire. *Eng Struct* 2022;266:114584.
- [70] EN 1992-1-1. Eurocode 2: Design of concrete structures — Part 1-1: General rules and rules for buildings. Brussels: European Committee for Standardisation; 2004.
- [71] AASHTO. AASHTO LRFD bridge design specifications. fourth ed. Washington, D.C.: AASHTO; 2007.
- [72] Raza S, Widmann R, Michels J, Saidi Saïdi M, Motavalli M, Shahverdi M. Self-centering technique for existing concrete bridge columns using prestressed iron-based shape memory alloy reinforcement. *Eng Struct* 2023;294:116799. <https://doi.org/10.1016/j.engstruct.2023.116799>.
- [73] Hosseini F, Gencturk B, Jain A, Shahzade K. Optimal design of bridge columns constructed with engineered cementitious composites and Cu-Al-Mn superelastic alloys. *Eng Struct* 2019;198:109531. <https://doi.org/10.1016/j.engstruct.2019.109531>.
- [74] Raza S, Menegon SJ, Tsang H-H, Wilson JL. Force-displacement behavior of limited ductile high-strength RC columns under bidirectional earthquake actions. *Eng Struct* 2020;208:110278. <https://doi.org/10.1016/j.engstruct.2020.110278>.
- [75] Raza S, Menegon SJ, Tsang H-H, Wilson JL. Axial load variation of columns in symmetrical rc buildings subject to bidirectional lateral actions in regions of low to moderate seismicity. *J Earthq Eng* 2022;26(5):2701–29. <https://doi.org/10.1080/13632469.2020.1772151>.
- [76] Raza S, Tsang HH, Menegon SJ, Wilson JL. Generalized loading protocols for experimentally simulating multidirectional earthquake actions on building columns in regions of low-to-moderate seismicity. *J Struct Eng (U S)* 2021;147(7). [https://doi.org/10.1061/\(ASCE\)ST.1943-541X.0003056](https://doi.org/10.1061/(ASCE)ST.1943-541X.0003056).
- [77] Raza S, Menegon Scott J, Tsang H-H, Wilson John L. Collapse performance of limited ductile high-strength RC columns under unidirectional cyclic actions. *J Struct Eng* 2020;146(10):04020201. [https://doi.org/10.1061/\(ASCE\)ST.1943-541X.0002772](https://doi.org/10.1061/(ASCE)ST.1943-541X.0002772).
- [78] Ou Y-C, Wang P-H, Tsai M-S, Chang K-C, Lee George C. Large-scale experimental study of precast segmental unbonded posttensioned concrete bridge columns for seismic regions. *J Struct Eng* 2010;136(3):255–64. [https://doi.org/10.1061/\(ASCE\)ST.1943-541X.0000110](https://doi.org/10.1061/(ASCE)ST.1943-541X.0000110).
- [79] Lee WK, Billington SL. Performance-based earthquake engineering assessment of a self-centering, post-tensioned concrete bridge system. *Earthq Eng Struct Dyn* 2011;40(8):887–902. <https://doi.org/10.1002/eqe.1065>.
- [80] Japan Road Association. Design specifications of highway bridges, Part V seismic design. Maruzen, Tokyo, Japan; 2002.
- [81] Park, R. (1988). Ductility Evaluation from Laboratory and Analytical Testing-State of the Art.
- [82] Paulay T, Priestley M. Seismic design of reinforced concrete and masonry buildings. New York: Wiley; 1992.
- [83] Haselton, C.B., Liel, A.B., Lange, S.T., Deierlein, G.G. (2008) Beam-column element model calibrated for predicting flexural response leading to global collapse of RC frame buildings. Report no. PEER-2007/03,
- [84] ASCE/SEI. Seismic evaluation and retrofit of existing buildings. ASCE/SEI 41-17. Reston, VA: ASCE; 2017.